

# Improvement weldability of dissimilar joints (Ti6Al4V/Al6013) for aerospace industry by Laser beam welding

Anderson C. N. Clayton Nascimento Ribeiro (✉ [andersoncnribeiro@gmail.com](mailto:andersoncnribeiro@gmail.com))

Aeronautics Institute of Technology - ITA, São José dos Campos <https://orcid.org/0000-0001-5438-5506>

Rafael Humberto Mota de Siqueira

Institute of Advanced Studies - IEAv, São José dos Campos

Milton Sergio Fernandes de Lima

Institute of Advanced Studies - IEAv, São José dos Campos

Rafael Arthur Reghine Giorjão

Edison Joining Technology Center, The Ohio State University

Antônio Jorge Abdalla

Institute of Advanced Studies - IEAv, São José dos Campos

---

## Research Article

**Keywords:** Intermetallic compound, dissimilar joint, laser welding, titanium, aluminum

**Posted Date:** March 18th, 2021

**DOI:** <https://doi.org/10.21203/rs.3.rs-317480/v1>

**License:**  This work is licensed under a Creative Commons Attribution 4.0 International License.

[Read Full License](#)

---

Improvement weldability of dissimilar joints (Ti6Al4V/Al6013) for aerospace industry by  
Laser beam welding

Anderson Clayton Nascimento ribeiro<sup>1</sup>,

Rafael Humberto Mota de Siqueira<sup>2</sup>,

Milton Sergio Fernandes de Lima<sup>2</sup>;

Rafael Arthur Reghine Giorjão<sup>3</sup>,

Antônio Jorge Abdalla<sup>2</sup>

<sup>1</sup>Anderson Clayton Nascimento Ribeiro

ORCID: 0000-0001-5438-5506

[anderson.ribeiro10@fatec.sp.gov.br](mailto:anderson.ribeiro10@fatec.sp.gov.br)

1 Aeronautics Institute of Technology - ITA, São José dos Campos, São Paulo, Brazil

2 Institute of Advanced Studies - IEAv, São José dos Campos, São Paulo, Brazil

3 Edison Joining Technology Center, The Ohio State University, Ohio, USA

**Abstract** The discovery of new metal alloys and the technological advancement in welding processes are key resources for the aerospace industry to obtain cost reduction and better reliability. Thus, welded joints of dissimilar materials such as aluminum and titanium alloys has been explored due to its combined low density and high mechanical performance. Otherwise, welding of dissimilar metals may present deleterious factors to the welded joint as the formation of intermetallic and/or brittle second phase and residual stress. This project investigates the weldability of dissimilar welded joint (Al6013/Ti-6Al-4V) by Laser beam welding. The approach will be done in terms of mechanical properties and microstructural characterization. For this purpose, optimal laser offset from the joint line and the related heat input has been found. It was observed that offset controls the amount of the intermetallic compound layer in the fusion zone. Large pores were observed on the Al side of the weld metal when the offset is zero. The microstructure on the aluminum side consisted of  $\alpha$ -Al grains and the dispersed precipitates. Heat input and

offset also influenced in the volumetric fraction of the precipitates. Martensite  $\alpha'$  and secondary acicular  $\alpha$  phase was found in the titanium side. Furthermore, intermetallic compound of TiAl base phase such as TiAl,  $Ti_3Al_4$ , and  $Ti_2Al_3$  was formed. Tensile strength of welded joint was 60% of the Al alloy. In addition, for the same offset and higher heat input, there was an increase in the hardness of the interface.

**Keywords:** Intermetallic compound, dissimilar joint, laser welding, titanium, aluminum

## 1. Introduction

The use of dissimilar Al/Ti joints to obtain structures and components is a promising choice for the aerospace industry. In addition, there is also a growing application of dissimilar joints in the medical, shipbuilding, consumer goods, electronics and automotive sectors [1–3]. The combinations between the properties of aluminum and titanium alloys have advantages such as: increased corrosion resistance, better mechanical properties, reduced weight and cost of the structure or component [4, 5]. In this context, there are widely publicized studies on the replacement of riveting on aircraft fuselages by welding panels reinforced with stringers (welding of skin-stringer joints) to reduce the weight of the structure. Specifically, titanium-aluminum alloys are successfully applied to honeycomb sandwich and seat-track of aircraft panels [6].

Likewise, a study was made on the feasibility of hybrid structures consisting of aluminum, titanium and carbon fiber reinforced with polymeric matrix (CFRP) used in automobiles and aircraft [7], for example, in the protection panels of the lower wing skin panels and cargo door of the Boeing C-17, as well as in the junction of the wing constituted by Ti alloy with part of the fuselage of Al alloy [8]. Recently, research has been done on the use of Al/Ti joints in the frames of aero bodies and missiles [9].

The welding or brazing of dissimilar materials, in particular Al/Ti, is a challenging process, considering the different properties between the alloys, such as: crystalline structure, melting temperature, thermal conductivity and thermal expansion coefficient [10]. Another important feature is that both Ti and Al alloys have high chemical activity,

the result of which is that the oxide formed is not conducive to the junction interface between the two alloys (Al/Ti) and may produce slag in the inside the weld [11] and form  $\text{TiO}_2$  and  $\text{Al}_2\text{O}_3$  on the surface. It also results in layers of intermetallic compounds (IMCs) and/or other deleterious phases at the welded joint interface as a consequence of the chemical, physical and metallurgical differences of the dissimilar metals and according to the Al/Ti phase diagram, these being the main BMIs:  $\text{Ti}_3\text{Al}$ ,  $\text{TiAl}$ ,  $\text{TiAl}_2$  e  $\text{TiAl}_3$  [2, 12–14].

Several welding/brazing processes and techniques have been studied in order to control the precipitation of IMCs in the joint region. Vacuum diffusion joining process was used in Al/Ti alloys applying aluminization to the Ti plate surface, resulting in increased formation time for the intermetallic layer at the Al/Ti. By controlling the diffusion parameters, it was possible to reduce the formation of intermetallic [15]. Furthermore, Havlík et al. conducted a study on the weldability of the Ti-6Al-4V/AA 6061 dissimilar joint obtained by the electron beam process by varying the beam offset. The author reported the presence of  $\text{Ti}_3\text{Al}$ ,  $\text{TiAl}$ ,  $\text{Ti}_5\text{Al}_{11}$  and  $\text{Ti}_3\text{Al}_5$  as well as volume fraction of IMCs controlled by the offset variation [16].

Solid-state welding processes, including: explosion welding, friction stir welding [17–20], friction welding [21] and ultrasonic welding [22] were also evaluated for the Al/Ti scenario, however, these processes techniques have limitations as to joint configuration and structure size. All the welding or soldering-brazing processes studied, still need improvement due to the complexity of the factors involved because they may have low joint strength, dimensional limitation, high cost and impracticability for large-scale production.

Laser welding has been widely applied due to the high energy density, fast processing speed, less thermal deformation, and low distortions of the parts. In addition, proper heat input and laser offset capable of suppressing metallurgical reactions, such as formation of IMCs [1, 23, 24]. However, the weld bead's appearance and the stability of the process depend on several factors such as the low wettability/spreading of aluminum on titanium.

Casalino et al. evaluated the formation of IMCs in Al/Ti dissimilar joints achieved by fiber laser offset welding where no filler metal was used. Also identifying the influence of the morphology of the IMCs with the mechanical properties of the joint [25].

Song et al. evaluated the mechanical and microstructural properties of Ti6Al-4V/A6061 joint by laser brazing without filler metal. Good surface quality was obtained, and through the process parameters, it was possible to reduce the intermetallic layer formation, followed by an increase the tensile strength by 64% compared base metal [27]. Vaidya et al. performed laser welding, without filler metal, between AA6056 and Ti-6Al-4V alloys using a U-shaped chamfer technique on one interface. By using optimal welding parameters, it was possible to reduce the intermetallic layer,  $TiAl_3$ , and reduce crack propagation in fatigue conditions [28].

This study proposes to investigate and optimize the mechanical performance of the dissimilar butt joint obtained by the laser fiber welding, between the AA 6013-T4 aluminum alloy and the Ti-6Al-4V titanium alloy, both used in the aerospace industry. It was identified the influence of welding energy and offset (distance between laser spot and plates interface) with the microstructure, intermetallic compounds, and mechanical properties of the welded joint.

## **2. Materials and methods**

### **2.1 Materials**

The experiments were carried out using two different metal alloy plates, the aluminum class AA 6013-T4 and the titanium alloy Ti-6Al-4V - Grade 5, both plates with dimensions of 100 mm x 50 mm x 1.6 mm. The T4 description of the aluminum plate corresponds to a tempering designation, in which the aluminum alloy was subjected to the solubilization cycle, rapid cooling, and natural aging. The titanium sheet was used as received (obtained by the rolling process and subjected to the annealing heat treatment according to ASTM B265). The rolling direction was preserved for both, the aluminum alloy plate

and the titanium alloy plate. Table 1 shows the chemical composition and Table 2 shows the mechanical properties of the alloys used in the research.

**Table 1** - Chemical composition of base metal, wt%

	Al	C	Fe	Ti	V	Mn	Si	Cu	Mg	Cr	Zn
Ti6Al4V*	5.72	0.06	0.37	Base	4.00	-	-	-	-	-	-
AA 6013**	Base	-	0.50	0.10	-	0.80	1.00	1.00	1.20	0.10	0.25

\*According to the manufacturer

\*\*Ref.[29]

**Table 2** - Mechanical property

Alloys	Tensile strength (MPa)	Yield stress (MPa)	Modulus of elasticity (GPa)	Elongation (%)
AA 6013 - T4 [Ref.[30]]	350 ± 2	230 ± 2	53 ± 16	28 ± 1
Ti-6Al-4V [Ref.[31]-[32]]	895	830	114	10

## 2.2 Welding procedure

The welding experiments were carried out using the Laser Welding equipment, IPG, YLR-2000 Model located at the Multi-User Laboratory for the Development of Laser and Optics Applications of the Photonics Division (EFO) of the Institute for Advanced Studies (IEAv). The equipment offers 2 kW continuous laser of medium power, the active medium being a fiber coated with Ytterbium, output with 50 µm diameter, Beam Parameter Product (BPP) equal to 6.3 mm.mrad, and 5 m in length. The laser wavelength is 1.07 µm, beam quality ( $M^2$ ) of approximately 1. Gaussian distribution intensity TEM<sub>00</sub> [33] and a beam diameter of 0.1 mm. The details of the processing station where the laser is inserted is shown schematically in Figure 1.

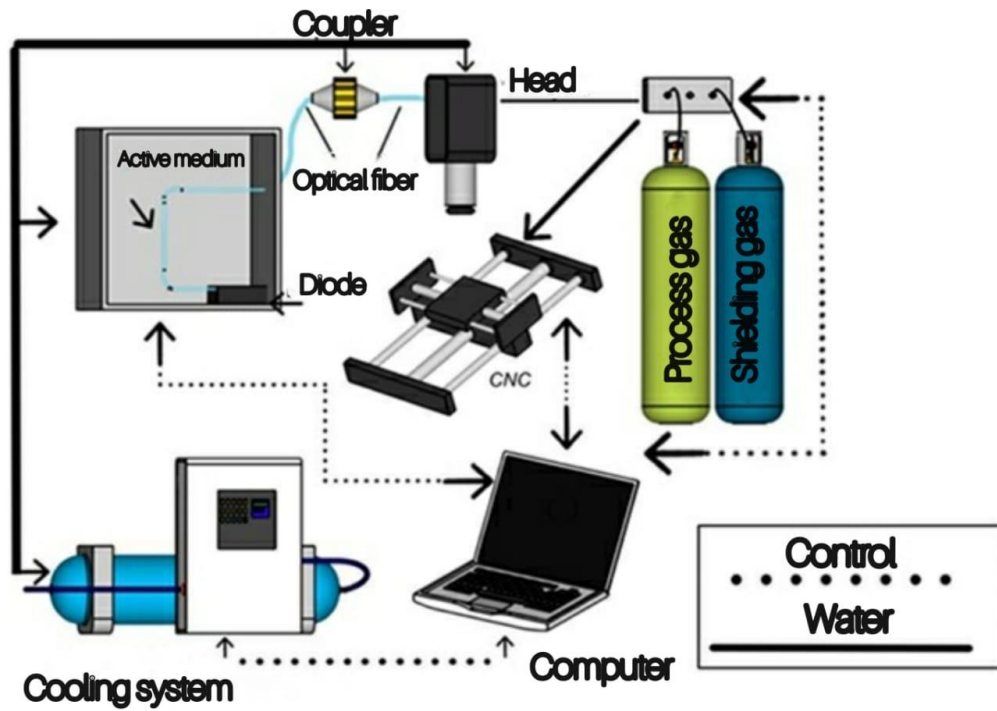


Figure 1 - Schematic diagram of processing station with fiber laser

During welding process, argon was used as a shielding gas with a flow rate of 18 l/min. The welding parameters on the are shown in Table 3.

Table 3 - Laser welding process parameters.

Conditions	Power (kW)	Welding speed (m/min)	Offset (mm)	Remarks
T1	1.2	2.0	0.5/Ti side	good bonding, welded at face and root only
T2	1.0	2.0	0.5/Ti side	weak bonding, welded at face only
T3	1.2	3.0	0.5/Ti side	no bonding
T4	1.0	3.0	0.5/T side i	no bonding
T5	1.2	2.0	0.3/Ti side	weak bonding, welded at root only
T6	1.0	2.0	0.3/Ti side	good bonding, welded joint
T7	1.2	3.0	0.3/Ti side	weak bonding, welded at face and root only
T8	1.0	3.0	0.3/Ti side	weak bonding, welded at root only
T9	1.0	1.0	0.5/Ti side	good bonding, welded joint
T10	1.5	1.0	0.8/Al side	no bonding
T11	1.5	1.0	0.8/Ti side	no bonding
T12	1.5	1.0	0.5/Ti side	no bonding
T13	1.50	1.0	Al/Ti interface	no bonding,

### 2.3 Microstructure characterization

Sample for microstructural characterization were taken from cross sectioned perpendicularly to the welding direction. All of them were mounted in bakelite. Hence, mounted samples were wet ground on progressively finer grades of SiC (240, 400, 600 and 1200, respectively) impregnated emery paper using copious amounts of water both as a lubricant and as a coolant. Afterward the samples were polished using 3 and 1-micron diamond solution, respectively. After a short time, the polished samples were

etched using Kroll reagent (10 ml of hydrofluoric acid, 45 ml of nitric acid and 45 ml of water) for times varying from 1 to 5 seconds. The etched samples surface was analyzed an optical microscope, Zeiss Axio Imager Z2m, and photographed. For scanning electron microscopy (SEM) an electron microscope SEM – FEG Inspect50 with secondary, backscattered electrical detectors, EDS X-ray spectrometer and backscattered electron diffraction EDAX camera (EBSD - TEAM), of the Laboratório de microscopia Eletrônica e de Força Atômica (LabMicro – USP), was used.

## **2.4 Hardness test**

An analysis of the hardness in the welded joint was obtained by microindentation, Vickers hardness test HV 0.2, carry out an automated Durascan 50 (Emcotest., Kuchl, Austria) to map the hardness distribution in a preselected area.

## **2.5 Tensile test**

Tensile specimens were cross-sectioned perpendicular to the welding direction and the tensile tests were accomplished on small size specimens according to ASTM E 8M - 04 standard [34]. For this purpose, it was used a testing machining EMIC DL-10000 with a maximum load capacity of 100 kN. Five samples were tested for each welding condition, and the average value was used to evaluate the tensile strength of the joint.

# **3. Results**

## **3.1 Weld bead profile**

The joint's cross- section images corresponding to conditions T1, T2, T6, T7, T8 and T9 are shown in Figure 2. Only these conditions showed sufficient strength in the welded joint to not break when handled and withstand the efforts submitted during the inlay procedure. It is observed that the molten zone is more extensive on the top, and narrower on the root. This indicates greater absorption of the incident radiation on the top of the

joint (side of the titanium plate). From the above, it was observed that the welding conditions adopted produced welds with full penetration for the side of the titanium alloy and met class A of the AWS D17.1 standard [35]. Except for the conditions T2 and T8, which weld beads showed discontinuity along the interface, with a weak joint formed on the top of the joint, as well pores in the molten area on the side of the titanium alloy.

Furthermore, the pores formed on the lower half of the weld bead (as in the case of sample T2) were caused by a non-constant geometry of the keyhole cavity [36]. This region, close to the keyhole bottom wall (RKW - rear keyhole wall) is maintained by the convection and reflection of thermal energy through the transported steam metal.

A notable behavior in the molten zone of the aluminum alloy for sample T8 was the formation of pores, especially in the center of the Al/Ti interface. As already mentioned, the fusion of the aluminum alloy took place through the thermal energy emanated by conduction and radiation from the keyhole formed in titanium. It is known that the trapping of hydrogen or a shielding gas is the main factor for the formation of pores in the weld is due to the fast cooling speeds of the molten metal [37]. Furthermore, the aluminum alloy elements have a low boiling point and lower viscosity of the molten metal than the titanium alloy. This promotes rapid fluctuations in the liquid metal which may cause discontinuities in the Al/Ti interface of the welded joint, such as the voids and bubbles that were observed (see Figure 2)

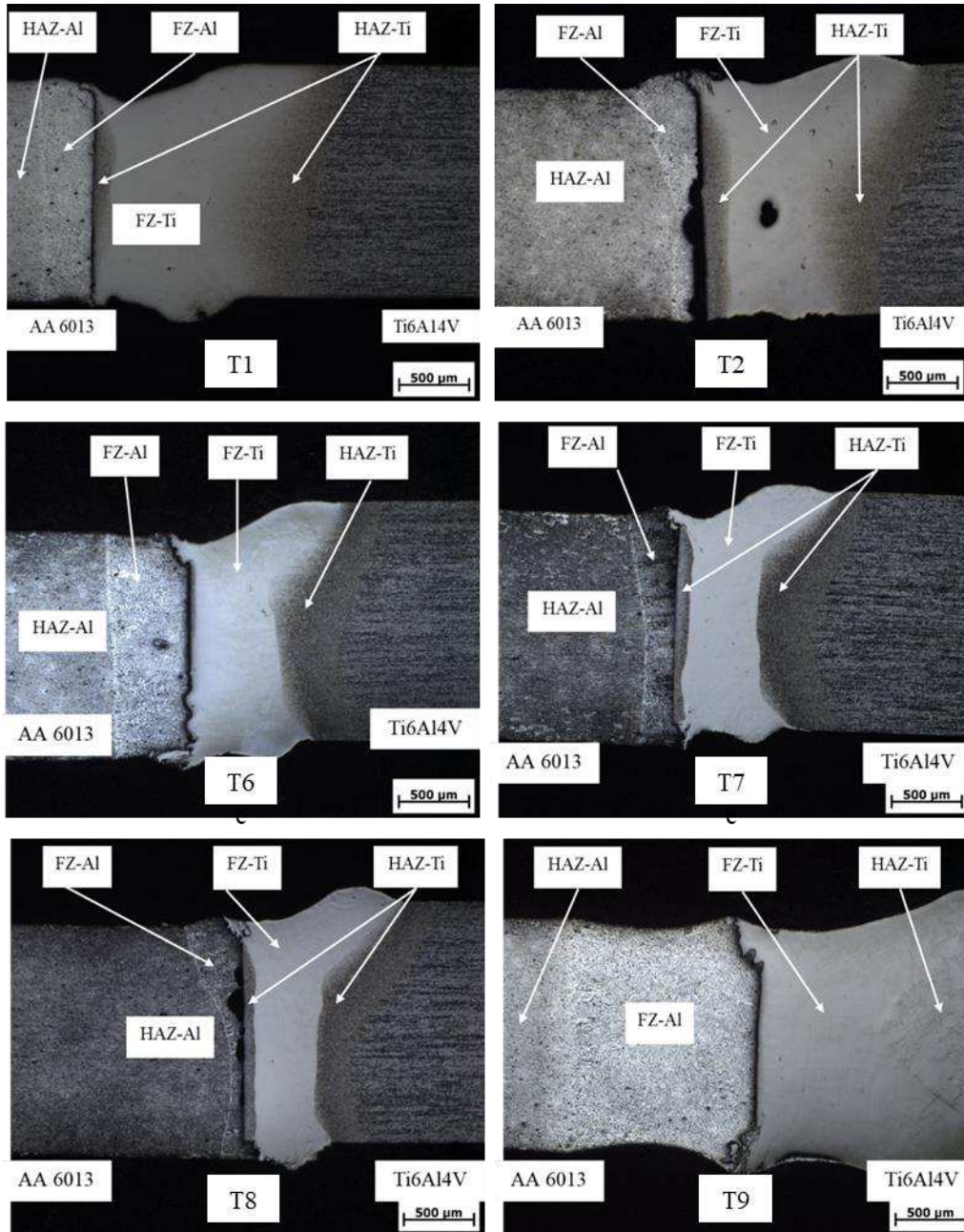


Figure 2 - Details of the dissimilar joint of the samples: T1, T2, T6, T7, T8 and T9. Showing the region of the heat affected zone (HAZ) and fused zone (FZ). Original magnification 25x

T9 sample, shown in Figure 2, exhibited the most extended FZ and HAZ compared to other conditions. Also, melting of both aluminum and titanium at the Al/Ti interface of the welded joint was observed, and consequently, a better wettability of aluminum in

titanium obtained. Even though condition T9 suffered the same welding energy and the same offset as condition T2, the value of the welding speed was half of T2. The welding speed and beam intensity, or laser power, affected the weld bead geometry and quality.

### **3.2 Effect of heat input and offset on microstructure**

As mentioned above, HAZ extent, volume of the molten metal, the volumetric fraction of the phases present and the intermetallic compounds are associated with the value of the offset and the welding energy used in each condition of the experiments. Likewise, the appearance of the weld bead is closely related to the action that the molten metal has to wet the top of the titanium alloy. This characteristic agrees with other brazing experiments on dissimilar joints [8].

Considering the cases in which the offset was assigned to the side of the titanium alloy, that is, the laser beam focused on the titanium plate, at certain distances from the Al/Ti interface, only in this phenomenon did the phenomena responsible for the formation of the keyhole occur. The aluminum was heated to a melting temperature by propagated conduction from the titanium side. Therefore, to calculate the welding energy (HI), the absorption coefficient of the titanium alloy, Ti-6Al-4V ( $A_{bs} = 0.4$ ), was used [38].

In laser welding, the welding energy (HI) is a function of the absorbed power ( $P_A$ ) and the welding speed ( $W_s$ ):

$$HI = \frac{P_A}{W_s} \quad (1)$$

The value of  $P_A$  corresponds to the product of the intensity of the beam that hit the plate and the average value of absorptivity [39]. Table 5 presents the values of the welding energy for each welding condition.

Table 4 – Heat input values

Sample	Power (kW)	Offset (mm)	Ws (mm/s)	HI (J/mm)
T1	1.20	0.5	33.3	14.4
T2	1.00	0.5	33.3	12.0
T5	1.20	0.3	33.3	14.4
T6	1.00	0.3	33.3	12.0
T7	1.20	0.3	50.0	9.6
T8	1.00	0.3	50.0	8.0
T9	1.00	0.5	16.6	24.0
T10	1.50	0.8Al	16.6	36.0
T11	1.50	0.8Ti	16.6	36.0
T12	1.50	0.5Ti	16.6	36.0
T13	1.50	0.0	16.6	36.0

Figure 4 shows the microstructure of the welded joint that includes the cross section of the top region, the center and the root of the weld bead. In all aluminum regions it is possible to observe that in the region of the HAZ, near the bonding zone, there is a partially fused region (PFZ), there are grains with elongated epitaxial growth, as well as equiaxial grains. Columnar grains grew epitaxially from the fusion line, while equiaxial grains were formed in the liquid phase above the direction of solidification due to constitutional sub-cooling [40].

In Figure 4 (a) the existence of solidification cracks along the dendritic grains in the melted area were found. Cracking by solidification occurs when residual tensile stresses (due to the action of high temperature) are induced by the internal contraction and the external displacement of the weld metal, exceeding the flow limit of the weld metal within a fragile temperature range.

The value of the extension of the partially molten zone, for the T1 and T2 conditions, are close (72.5 and 74  $\mu\text{m}$  respectively), which corresponds to two or three grains, according to the literature [41]. However, the average grain size in T1 is 83%

larger than the average grain size in T2. This fact is associated with the different values of the welding energy in these conditions. Knowing that the increase in welding energy slows down the cooling rate, and tends to increase the grain size, Figure 4 (b) indicates the region where there possibly is the formation of an intermetallic compound for condition T1.

In Figure 4 (c, d) we observe the image of the microstructure of the central region of the cross section to the welded joint for sample T1. Through the analysis of the images, it was found that, in the center of the weld, there was no formation of the reactive layer at the interface (RLI) or any other coalescence mechanism. Likewise, this fact occurs under the conditions shown in Figure 6. Figure 5 shows the transition region between the HAZ (coarse grains) and the molten zone of the aluminum alloy. The image shows the  $\alpha$ -Al grains and the presence of distributed precipitates (dark spots), in addition to the growth of cellular dendritic grains.

Figure 6 (d) highlights the discontinuities in the molten zone of the aluminum alloy, at the vicinity of Al/Ti contact interface (central region of the weld cross section, condition T8), in addition to the distinct morphology and size of the  $\alpha$ -Al grains, when comparing them with all conditions of the same offset value. The molten zone is characterized by coarse dendritic grains, segregated interdendritic phases and with the absence (or reduction) of hardening phases [42, 43].

Figure 7 (a) shows the base metal microstructure of the Ti-6Al-4V alloy. It is observed that it consists of a matrix of  $\alpha$  phase, which corresponds to the region of light color (with compact hexagonal structure), where the  $\beta$  phase is dispersed, which corresponds to the dark field (with the cubic structure of a centered body) [44].

The fused zone of the titanium side was practically unchanged, being formed by coarse columnar grains of previous  $\beta$ . Due to the fast-cooling rate, characteristic of the laser welding process, the martensitic transformation of  $\beta$  occurs, thus resulting in a fine needle-shaped microstructure. Figure 7 (b) depicts fused zone, a large percentage of  $\alpha'$  martensite, in addition to the secondary  $\alpha$  acicular phase. The formation of  $\alpha'$  occurred because the  $\beta$  phase did not have enough time to precipitate  $\alpha$ , that is, it was possible to transform the network parameter, however the  $\beta$  composition remained almost

unchanged, as a consequence:  $\alpha$  and  $\alpha'$  phases were formed through this transformation of the lattice parameter [45].

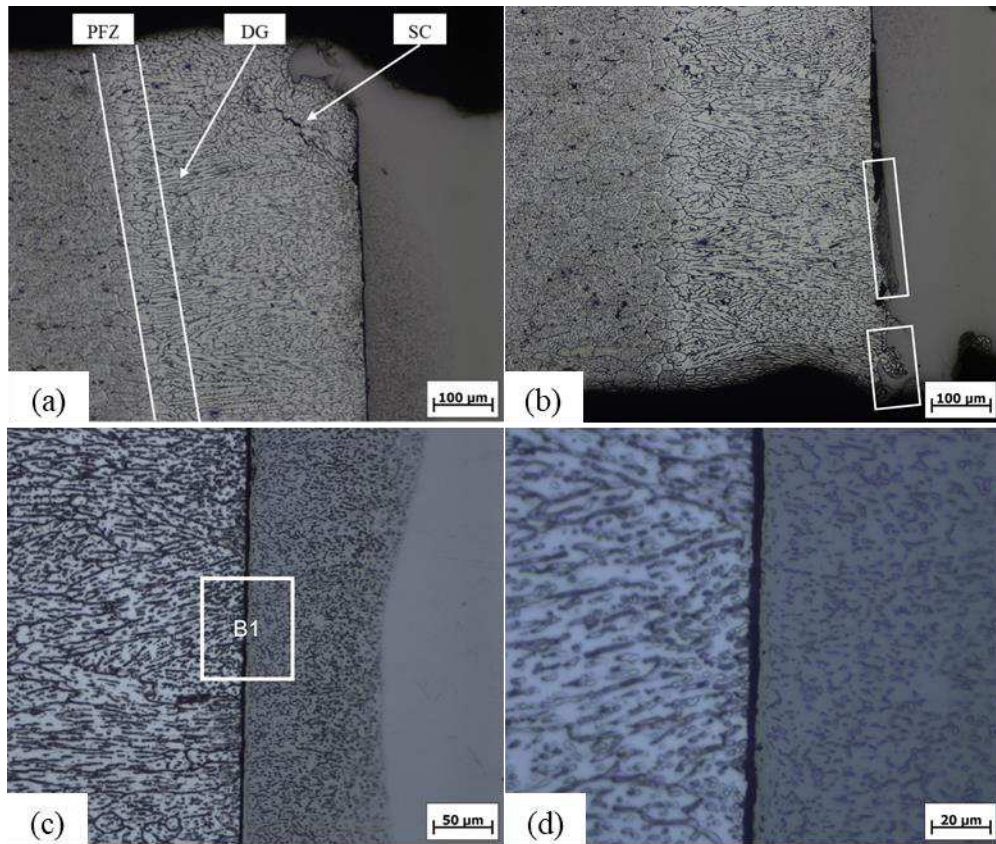


Figure 3 – Microstructural characteristic at the welded joint for the T1 condition: a) partially fused zone (PFZ), dendritic grains (DG), cracking by solidification (SC); b) possible regions of intermetallic compound in the root; c) center of the cross section, d) region B1, original magnification 200x

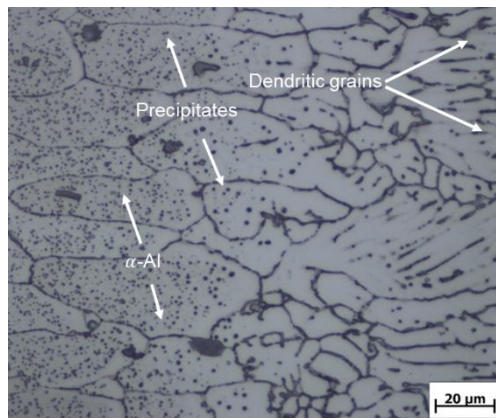


Figure 4: Sample T1, details at partially fused zone. Original magnification 500X

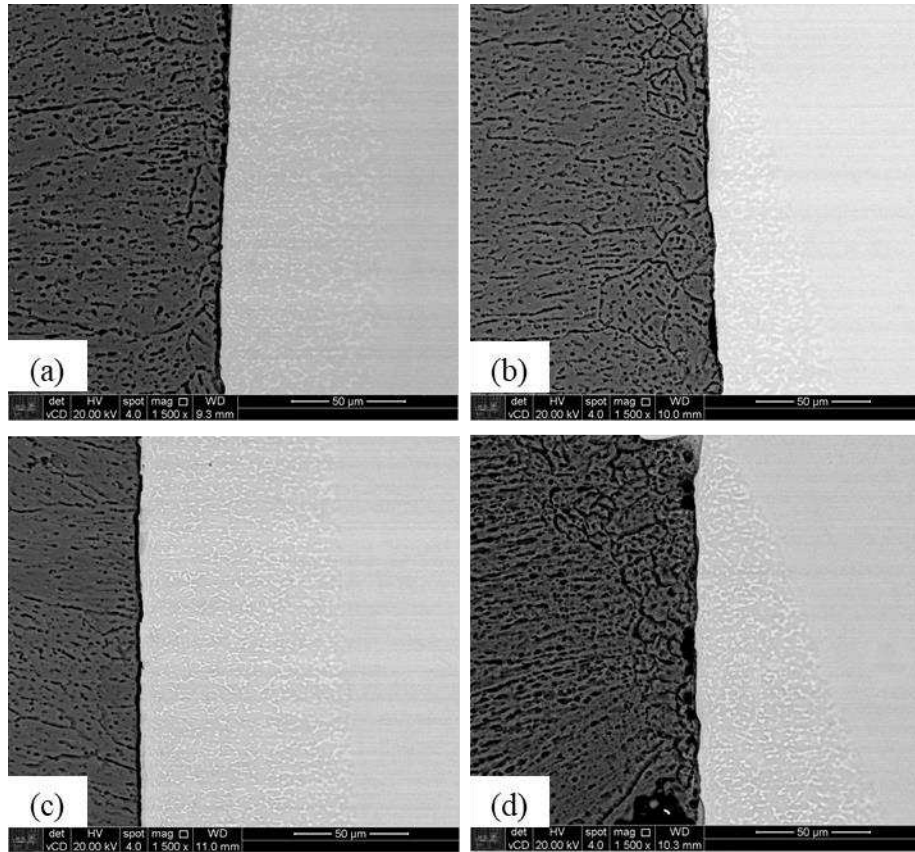


Figure 5 - SEM image of the joint cross section center: a) condition T5, b) condition T6, c) condition T7 and d) condition T8

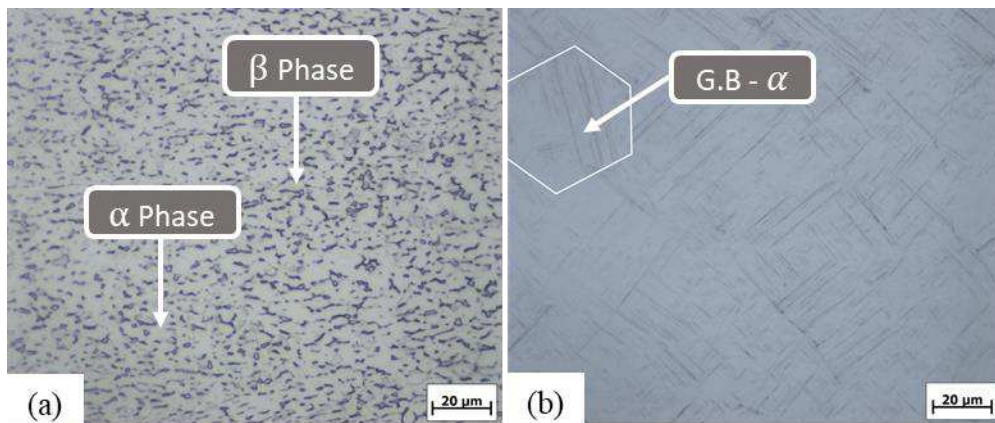


Figure 6 – a) Microstructure of the base metal - titanium alloy (Ti-6Al-4V), original increase of 500x. b) Microstructure of the fused zone of the titanium alloy (Ti-6Al-4V), showing the  $\alpha'$  grain contour, original magnification 500x magnification

The HAZ, close to the fused zone, was affected by a greater amount of thermal energy during the process, in which the temperature varied between 980 - 995 °C (transition temperature  $\beta$ ), and 1605 °C (solidus temperature). Therefore, the HAZ observed close to the FZ consisted mainly of the acicular martensitic phase  $\alpha'$  and a small amount of acicular  $\alpha$ , microstructures that are similar to that of the FZ [46, 47].

In each welding condition, different values of volumetric fraction of the  $\alpha$  phase in this region were found (using image software), for example: 13%, 18%, 32% and 18% for samples T5, T6, T7 and T8 respectively. Thus, the volumetric fraction of  $\beta$  in this region increased as it was subjected to higher values of heat input.

### **3.3 Formation of intermetallic compounds**

Through the results so far, and in accordance with other studies, it is clear that the characteristics, size, distribution and morphology of the phases formed in the laser welding process of the Al/Ti joint is administered by the coefficient of diffusion, welding energy, beam offset, and distance to the Al/Ti [48] interface. The diffusion coefficient of Ti in Al is  $2.15 \times 10^{-8} \text{ m}^2 / \text{s}$  [49] and it was observed that the phenomenon can occur at a relatively low temperature, around 600 °C [50].

The formation of intermetallic compounds was identified in the darkest gray regions, which can be seen in Figure 8 and Figure 9. In these places, either the aluminum alloy or the titanium alloy melted, or a composition of a reactive layer at the interface between Al/Ti occurred. It was identified in the images of the top, as well as the root, that the reactive layer of the interface is not homogeneous and tends to be curved. This behavior is related to the heat input and the interaction between the aluminum and titanium alloys in their liquid state.

Likewise, in the center of the welded joint shown in Figure 9 (b) (sample T9), a reaction layer was formed at the interface, in addition to the presence of the titanium lamellae that diffused in the aluminum where the temperature of recrystallization of aluminum was higher. The direction of growth of the lamellae followed that of the heat flow.

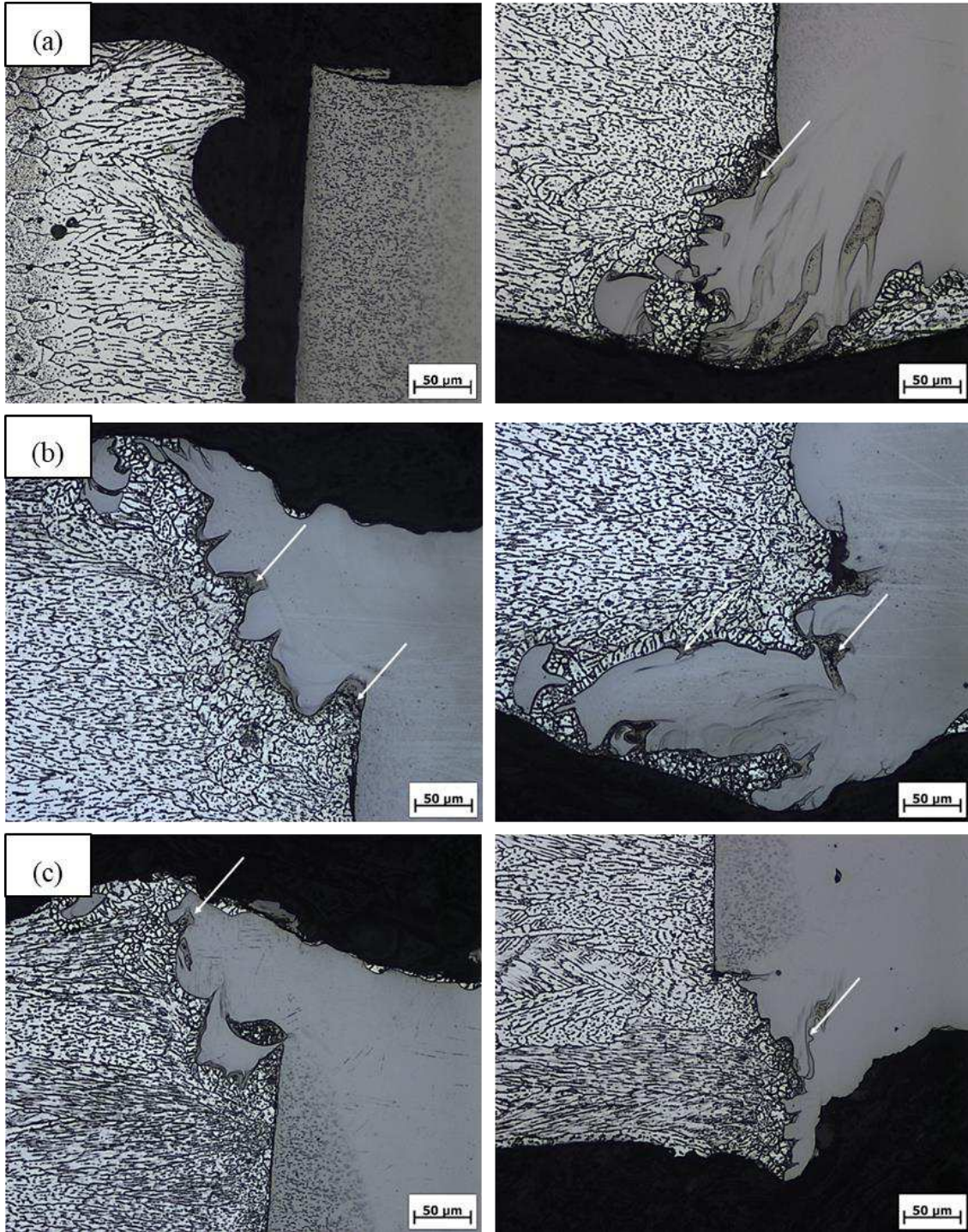


Figure 7 – Regions with intermetallic compounds: Face (left) and root (right) of welded joints, (a) - Sample T2, (b) - Sample T6 and (c) - Sample T7.

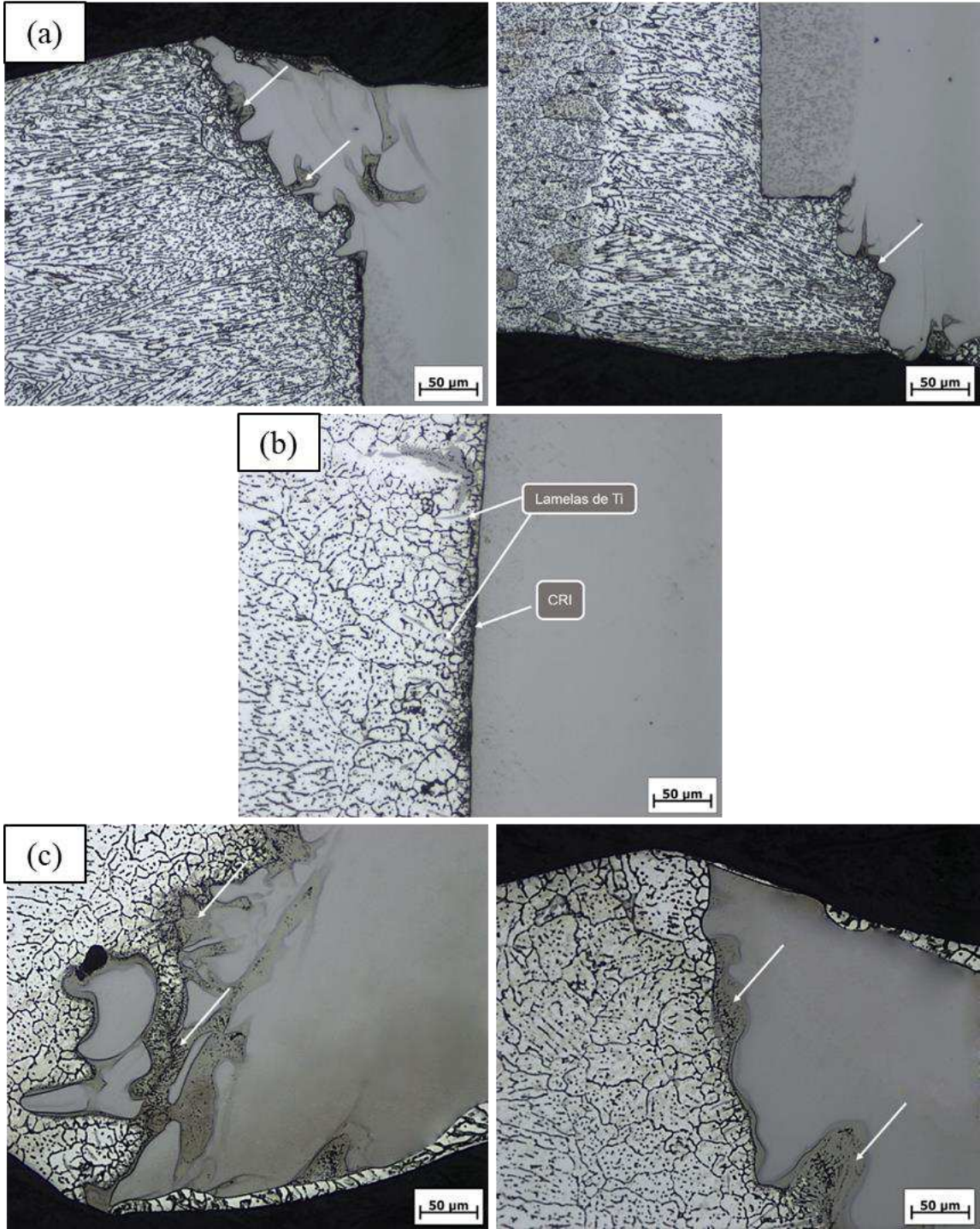


Figure 8 – Regions with intermetallic compounds: (a) - Face (left) and root (right) of the welded joint, Sample T8. (b) - Center of the joint, Sample T9 and (c) - Face (left) and root (right) of the welded joint, Sample T9

### 3.4 EDS Analysis

It can be seen the distribution of Al, Ti, V e Si elements along the course depicted at Figure 9 (a). Figure 9 (b) shows the results obtained by the EDS analysis across the Al/Ti welded interface.

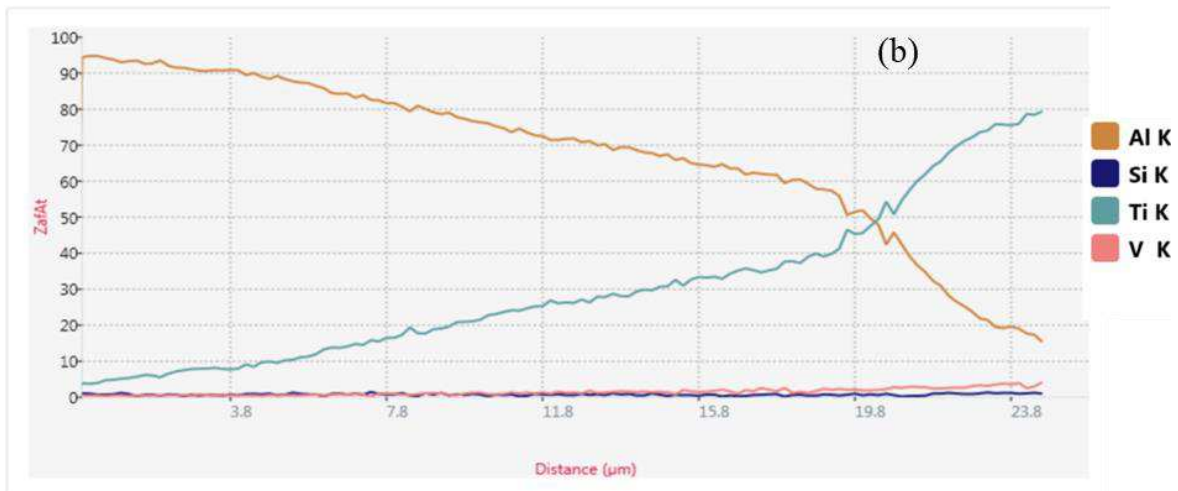
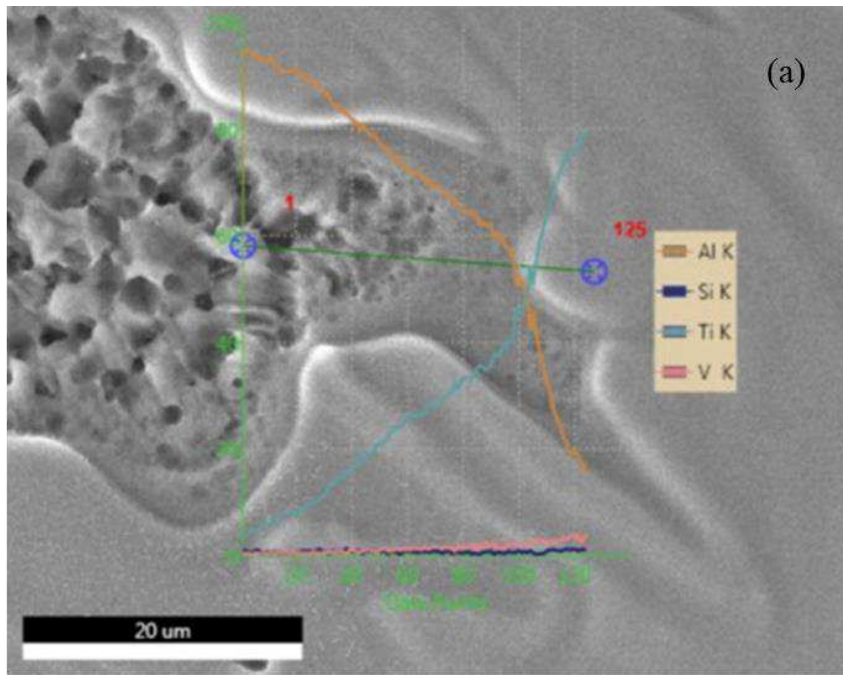


Figure 9 – (a) Weld metal interface with path that EDS was carried out (b) Results of EDS analysis across Al/Ti welded interface

Note the reduction of Al content as the line approaches to titanium alloy from the starting point of the analysis until 20  $\mu\text{m}$ , where a peak of the Ti content occurs. It was identified that this region corresponds to approximately 0.5  $\mu\text{m}$  layer. The presence of IMC could be assumed at this location. Furthermore, Table 9 shows the probable IMCs at each EDS analysis site measured at selected locations marked as Spectron of spots identified at Figure 10 according to the chemical compositions presented from Table 6 to Table 9.

Table 5 - Chemical composition measured at selected locations marked as spots 1 to 6, sample T6

Position	Al	Ti	V	Si
wt. % / at. %				
Spot 1	71.28 / 81.10	25.83 / 16.55	1.67 / 1.00	1.23 / 1.34
Spot 2	40.97 / 55.19	55.7 / 42.26	3.02 / 2.15	0.31 / 0.40
Spot 3	28 / 40.87	68.9 / 56.62	2.88 / 2.23	0.20 / 0.28
Spot 4	23.62 / 35.46	73.16 / 61.86	3.02 / 2.40	0.20 / 0.28
Spot 5	36.43 / 50.38	60.38 / 47.04	2.78 / 2.03	0.41 / 0.55
Spot 6	25.41 / 37.74	70.18 / 58.70	4.25 / 3.34	0.16 / 0.22

Table 6 – EDS analysis at the places indicated as spots 1 and 2, intermetallic layer, sample T7

wt.% / at. %				
Position	Al	Ti	Mg	Si
Spot 1	44.28 / 58.29	54.98 / 40.77	0	0.74 / 0.93
Spot 2	74.69 / 83.10	23.32 / 14.62	0.99 / 1.22	0.99 / 1.06

Table 7 – Chemical composition measured at selected locations marked as spots 1 and spot 2, sample T5

wt.% / at.%				
Position	Al	Ti	V	Si
Spot 1	44.54 / 58.74	51.97 / 38.60	3.10 / 2.17	0.39 / 0.49
Spot 2	37.24 / 51.30	59.65 / 46.28	2.86 / 2.09	0.25 / 0.33

Table 8 – Chemical composition measured at selected locations marked as spot 1 to spot 6, sample T8

wt.% / at.%						
Position	Al	Ti	Mg	Si	F	V
Spot 1	94.43 / 92.27	0.00	1.06 / 1.15	0.00	4.51 / 6.28	0.00
Spot 2	7.45 / 12.53	87.41 / 82.88	0.00	0.00	0.00	5.14 / 4.59
Spot 3	38.07 / 52.14	58.38 / 45.04	0.00	0.41 / 0.54	0.00	3.15 / 2.28
Spot 4	26.64 / 39.21	69.71 / 57.81	0.00	0.21 / 0.30	0.00	3.44 / 2.68
Spot 5	28.08 / 40.98	68.09 / 55.96	0.00	0.16 / 0.23	0.00	3.66 / 2.83
Spot 6	8.33 / 13.92	86.85 / 81.78	0.00	0.04 / 0.06	0.00	4.79 / 4.24

Table 9 – Identification of the intermetallic compounds

Point	Sample 6	Sample 7	Sample 5	Sample 8
1	Ti <sub>5</sub> Al	Ti <sub>2</sub> Al <sub>3</sub>	Ti <sub>2</sub> Al <sub>3</sub>	MgF <sub>6</sub>
2	Ti <sub>3</sub> Al <sub>4</sub>	TiAl <sub>5</sub>	TiAl	N.F.I*
3	TiAl			TiAl
4	Ti <sub>5</sub> Al <sub>3</sub>			Ti <sub>3</sub> Al <sub>2</sub>
5	TiAl			TiAl
6	N.F.I *			Ti <sub>6</sub> Al

N.F.I\*: It did not form intermetallic.

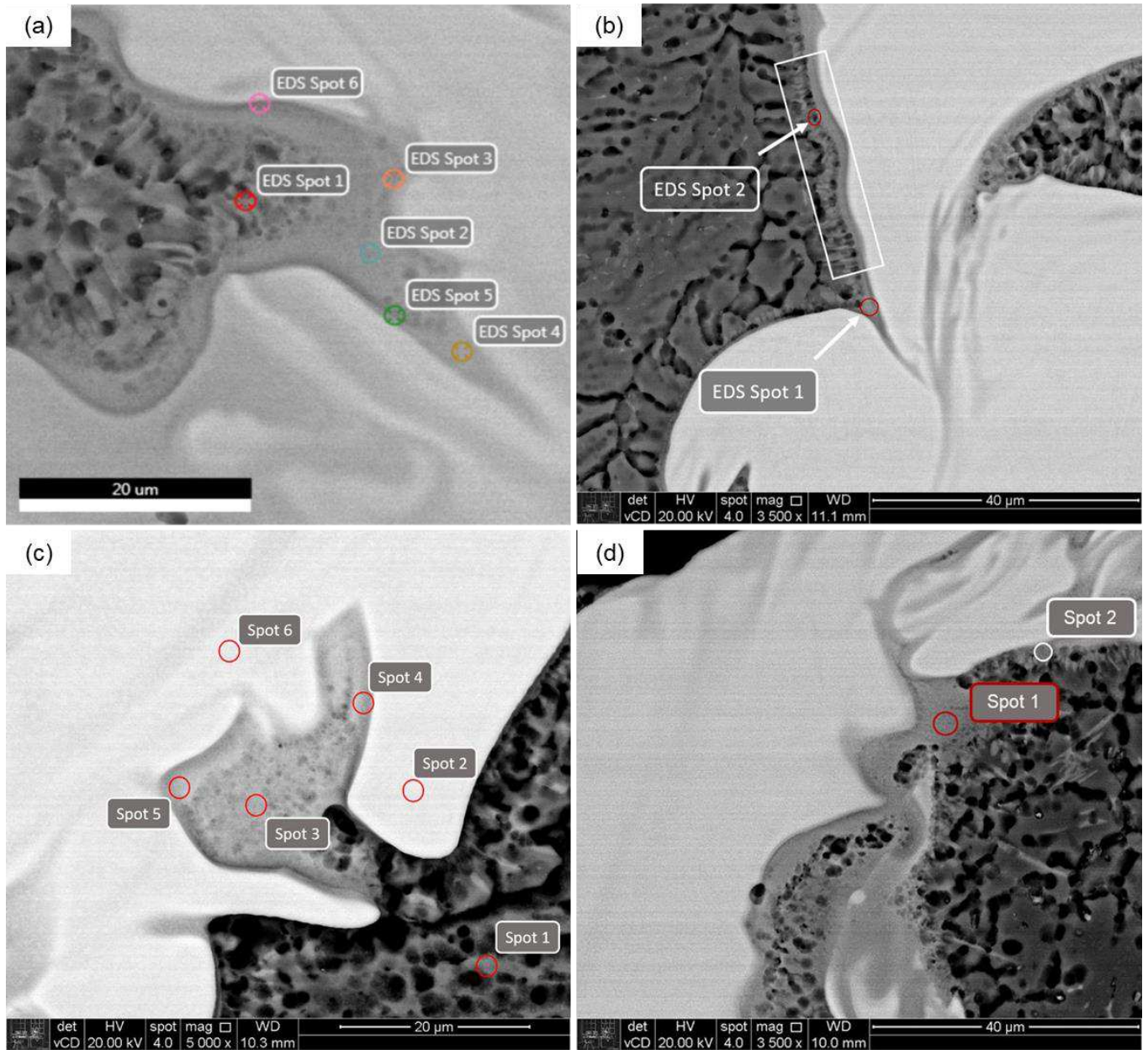


Figure 10 – Points EDS analysis performed at (a) sample 6, (b) sample 7, (c) sample 8 and (d) sample 5

Considering the Ti-Al phase diagram (Figure 14), the formation of the  $Ti_3Al$  ( $\alpha_2$ ) phase occurs in a composition range of 22 to 39% at. Al (14 to 19% wt). The phase is stable close to 1090 °C for Ti-25 Al (25%) stoichiometric composition and has a hexagonal  $DO_{19}$  crystalline structure. The  $TiAl$  phase ( $\gamma$  titanium aluminide) has an aluminum composition between 49 - 66% at, with a  $L1_0$  tetragonal centered face structure. The phase remains in order until its melting point (1440 °C) [51].

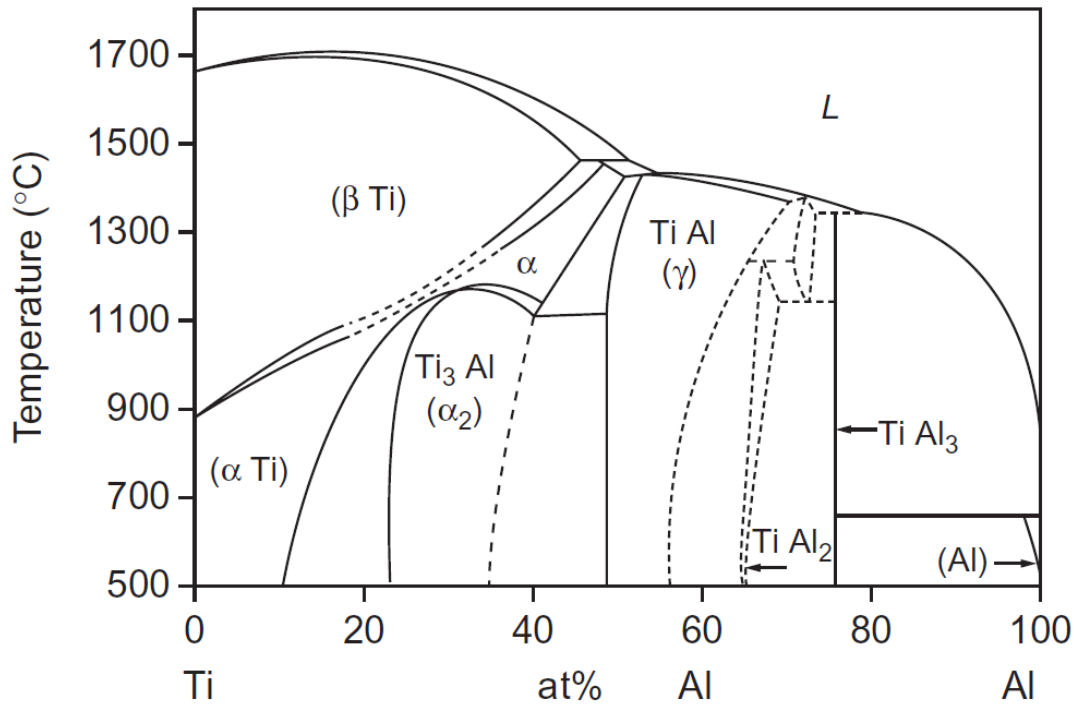


Figure 11 – Phase diagram of the Ti-Al system[52]

### 3.5 Tensile test

The results of the tensile tests, for the welding conditions adopted, are presented from Figure 13 to Figure 17. In Figure 13 we observe the average values of the maximum stress with the respective standard deviations for samples T1, T2, T5, T6, T7, T8 and T9. Note that conditions T6 and T9 exhibited the highest values of tensile strength, around 60 and 50%, respectively, of the tensile strength of the aluminum alloy (Table 11). In addition, the highest percentages of elongation also corresponded to conditions T6 and T9, being almost 6% of the initial length, as we can see in Figure 16 and Figure 17.

Furthermore, Figure 18 shows the behavior of the tensile strength as a function of the welding energy, considering an offset of 0.5 mm (Figure 18 (a)) and 0.3 mm (Figure 18 (b)), in that order. In both cases, it is noted that higher values of welding energy and offset tend to contribute to the increase in tensile strength, with a slight decrease in tension to 14 J/mm.

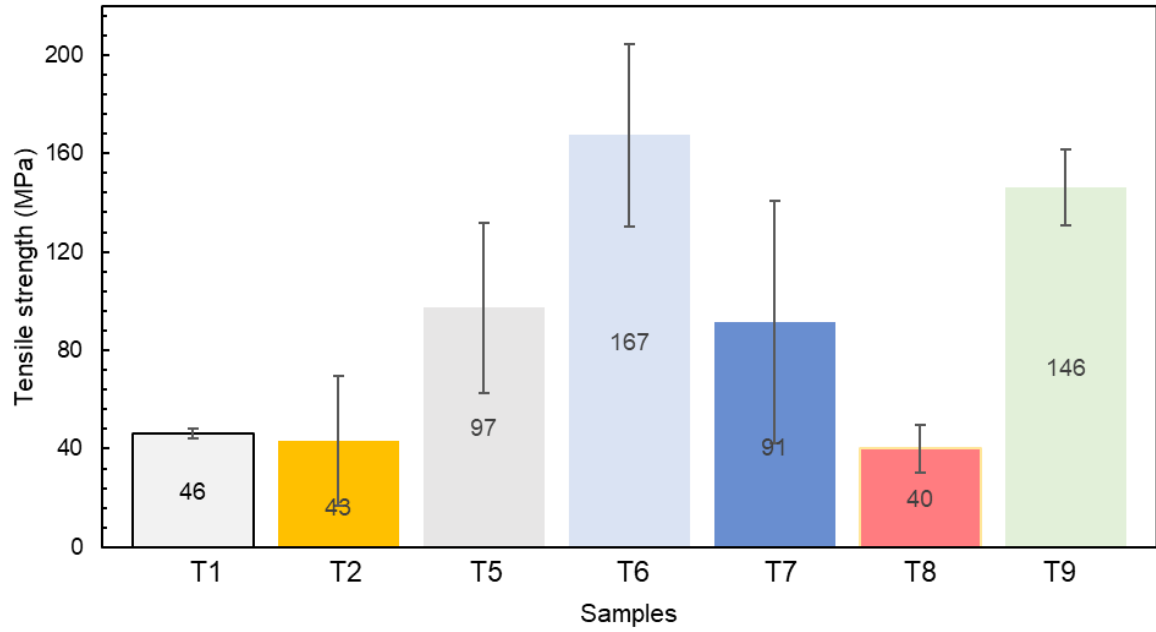


Figure 12 – Average value of maximum tensile stress for each welded condition

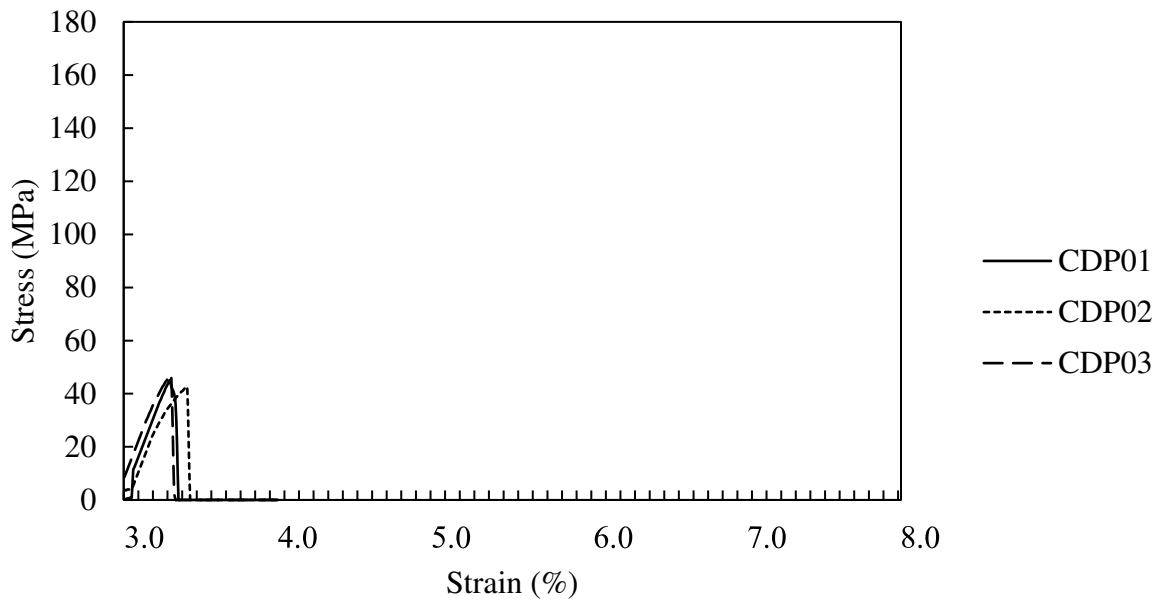


Figure 13 – Stress-strain curve - Sample T1

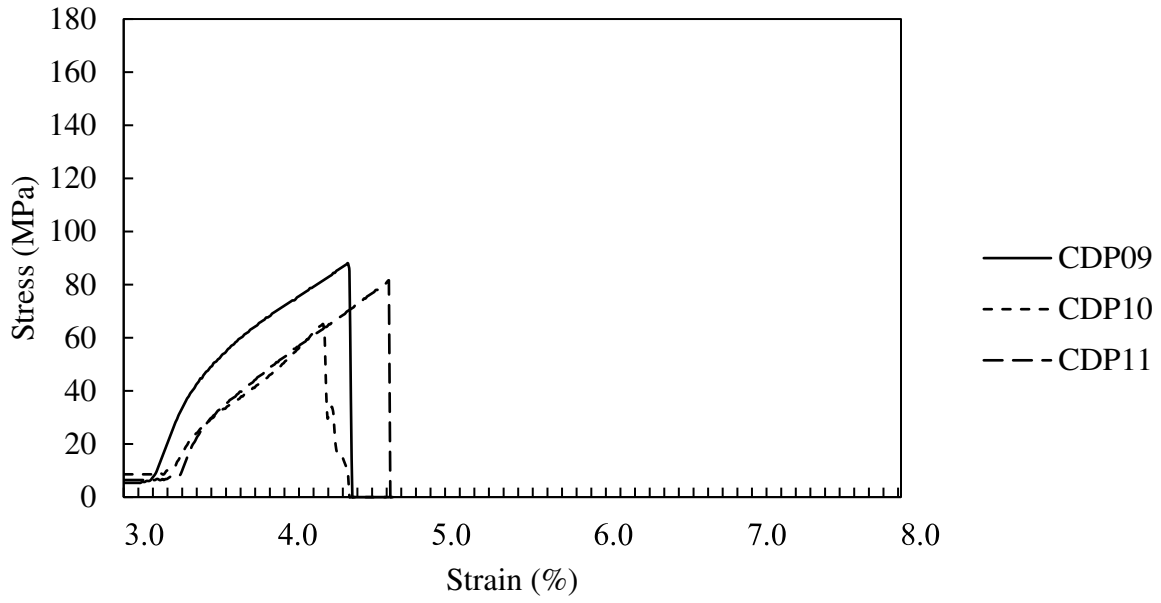


Figure 14 – Stress-strain curve - Sample T5

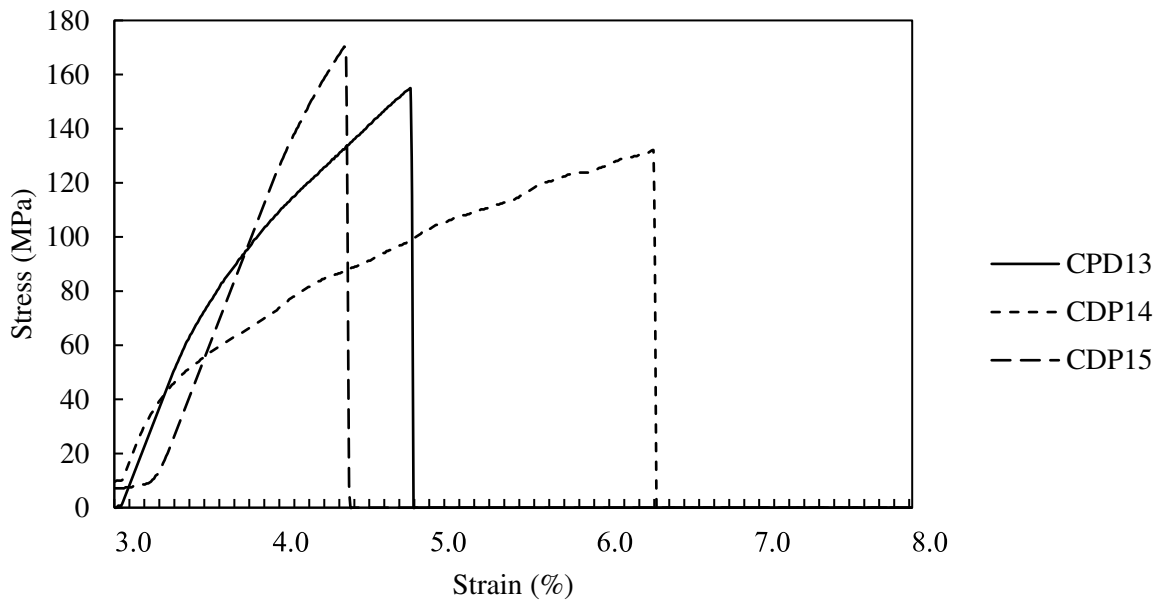


Figure 15 – Stress-strain curve - Sample T6

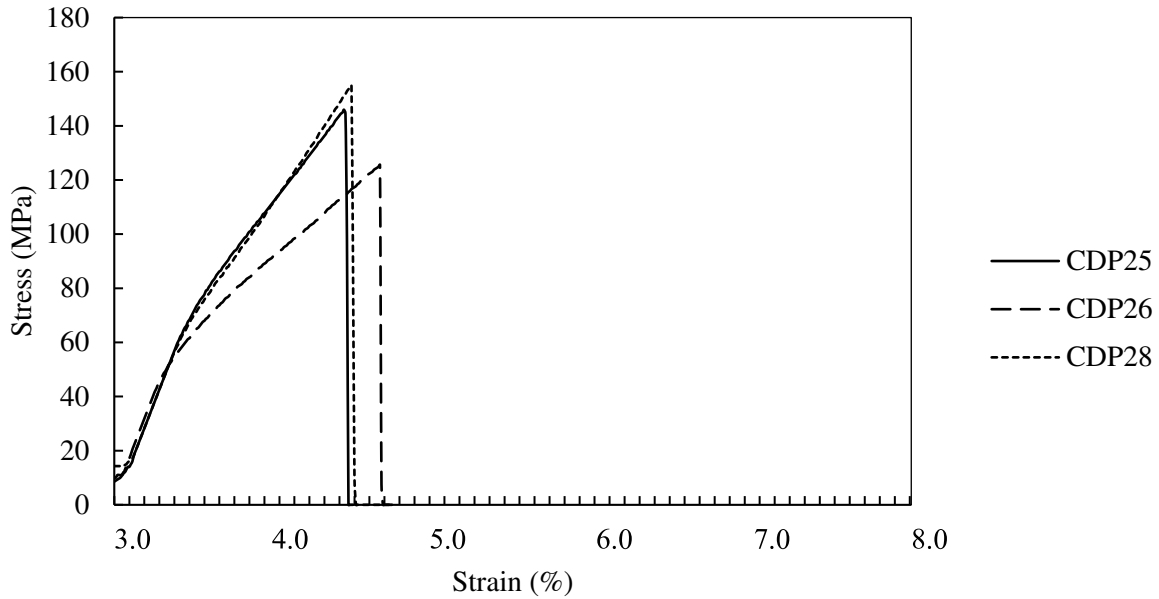


Figure 16 – Stress-strain curve - Sample T9

### 3.6 Hardness Test

The results of the hardness test on the dissimilar joint are presented from figure 19 to figure 21. The mapping of indentations can identify regions made of fragile phases, resulting from variations in the microstructure that form during the laser welding process. In order to better analyze the hardness map, the side of the aluminum alloy and the side of the titanium alloy next to the junction interface will be discussed separately.

#### 3.6.1 Aluminum alloy side:

Note that for the aluminum alloy side, in almost all conditions that were presented, the hardness in the region of the fused zone tends to increase as it moves away from the interface of the junction, even without changes in morphology and grain size. This is because the main hardening elements of the Al-Mg-Si alloy are Mg and Si. Mg evaporates during the welding process, due to its low melting point (650 °C) [53].

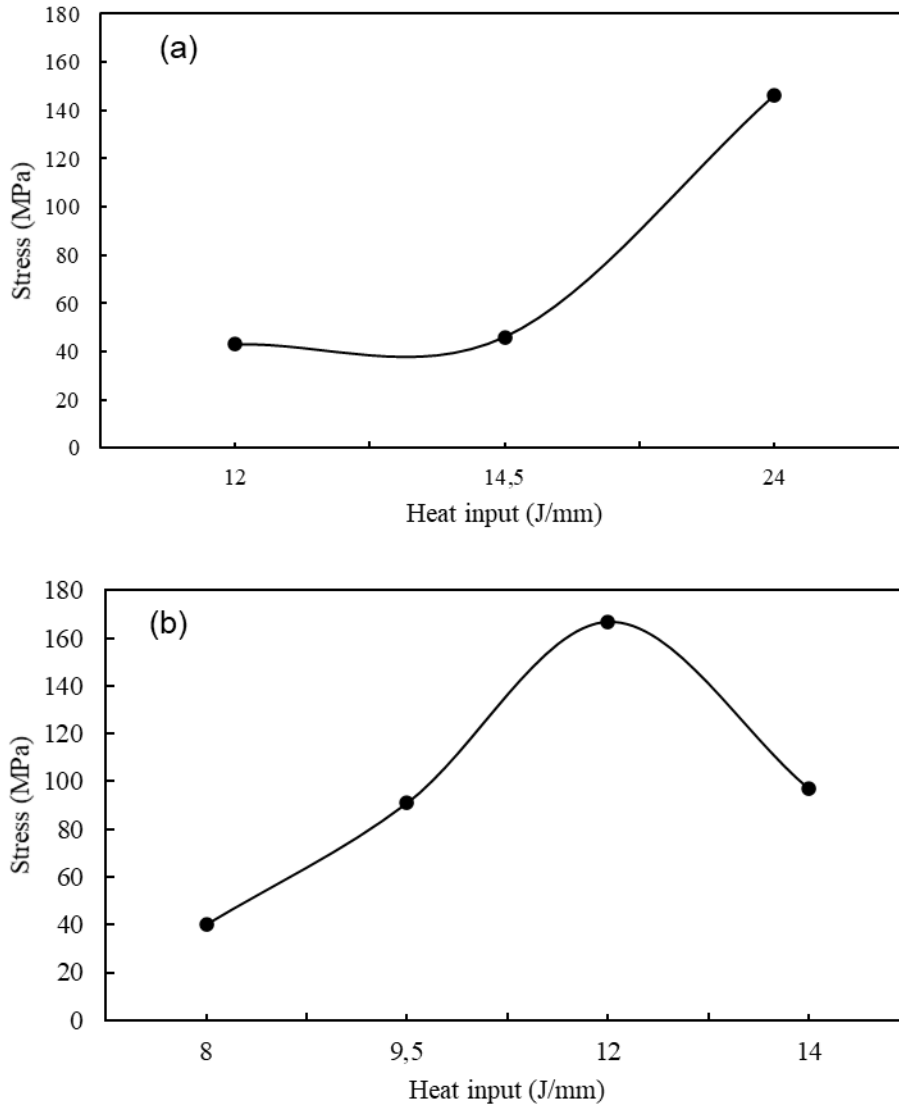


Figure 17 – Tensile strength as a function of heat input: (a) Welding conditions for offset = 0.5 mm. (b) Welding conditions for offset = 0.3 mm.

Approximately 0.3 mm from the interface (in the case of Sample 6), the loss of alloy elements such as Mg is reduced, as the energy received from the laser beam attenuates, resulting in increased hardness. Such behavior does not occur on the map corresponding to Sample 8. Where there is a discontinuity along the entire Al/Ti interface, in addition to the FZ with less than 0.05 mm in length. Sample 9 shows greater homogenization of the hardness values.

### 3.6.2 *Ti alloy side:*

The region analyzed for the titanium side covered the junction interface, the molten zone (FZ) and a part of the heat affected zone (HAZ), except in the case of samples 6 and 9 that did not present significant HAZ near the interface. It is observed in the indentation map for the side of the titanium alloy that the gradient of the hardness values is larger and more heterogeneous, comparing them with the side of the Al.

In addition, the presence of small sites of high hardness, close to the junction interface, indicates the formation of intermetallic compounds. This fact is clearly perceived at approximately 0.05 mm from the junction interface for sample 6 (top of the weld) and 0.2 mm for sample 9 (root of the weld). The highest hardness values in the molten zone occur due to the rapid cooling rate characteristic of the process, which results in a microstructure, consisting mainly of  $\alpha'$  martensite. On the other hand, the HAZ is formed by the  $\alpha/\beta$  phases that have less hardness. In general, the different hardness values occur due to the offset and welding energy used. The table below shows the points with the highest hardness values for each condition analyzed with the respective positions on the welded joint.

The hardness values for the junction interface have been significantly changed as a function of the offset and the welding energy. For the same offset value and higher welding energy value, there was an increase in the hardness of the interface. An example is sample 9, compared to sample 1, with almost twice the welding energy, the hardness value increased by 100 HV0.2.

Table 10 - Higher hardness values and their specific offset

Sample	Higher hardness value (HV0.2)	Location	offset (mm)/HI (J/mm)
1	442	~ 0.2 mm from the interface near to the root	0.5/14.4
5	506	~ 0.15 mm from the interface near to the root	0.3/14.4
6	520	~ 0.05 mm from the interface near to the face	0.3/12
7	589	~ 0.2 mm from the interface near to the root	0.3/9.6
8	506	~ 0.2 mm from the interface near to the root	0.3/8
9	570	~ 0.02 mm from the interface near to the root	0.5/24

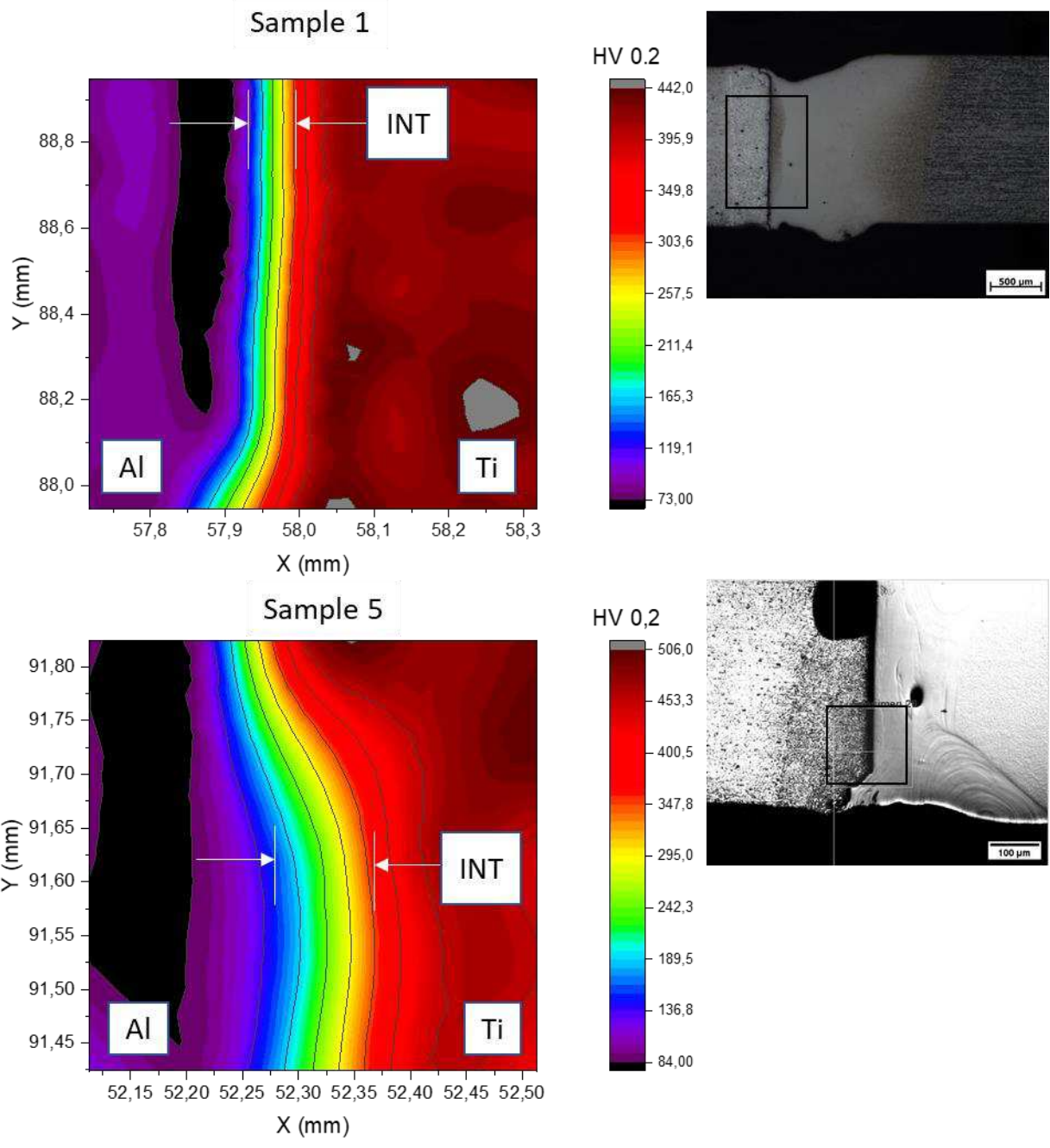


Figure 18 – Hardness values identified the analyzed regions and the interface of the test (INT) for the sample 1 and sample 5.

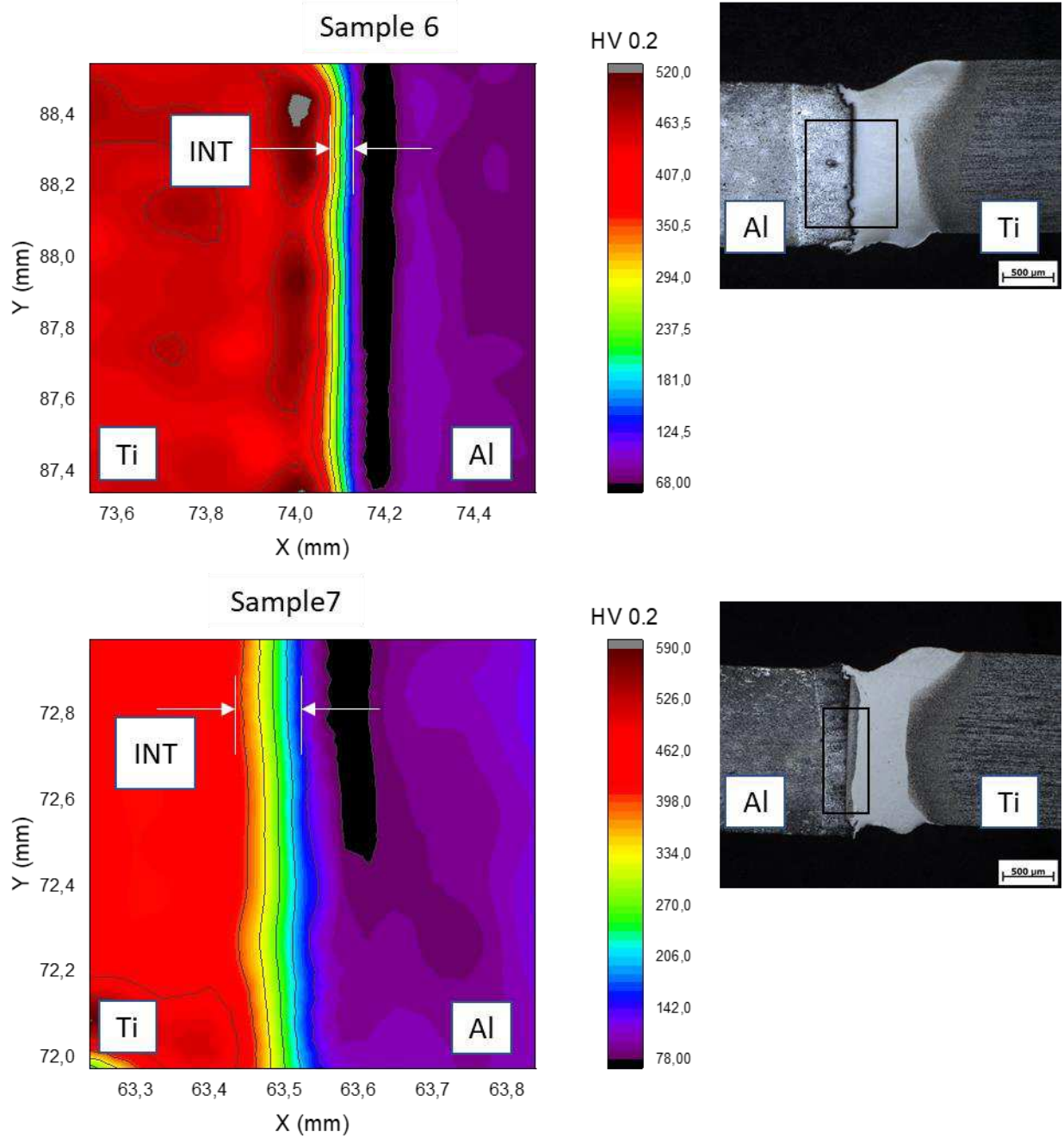


Figure 19 – Hardness values identified the analyzed regions and the interface of the test (INT) for the sample 6 and sample 7.

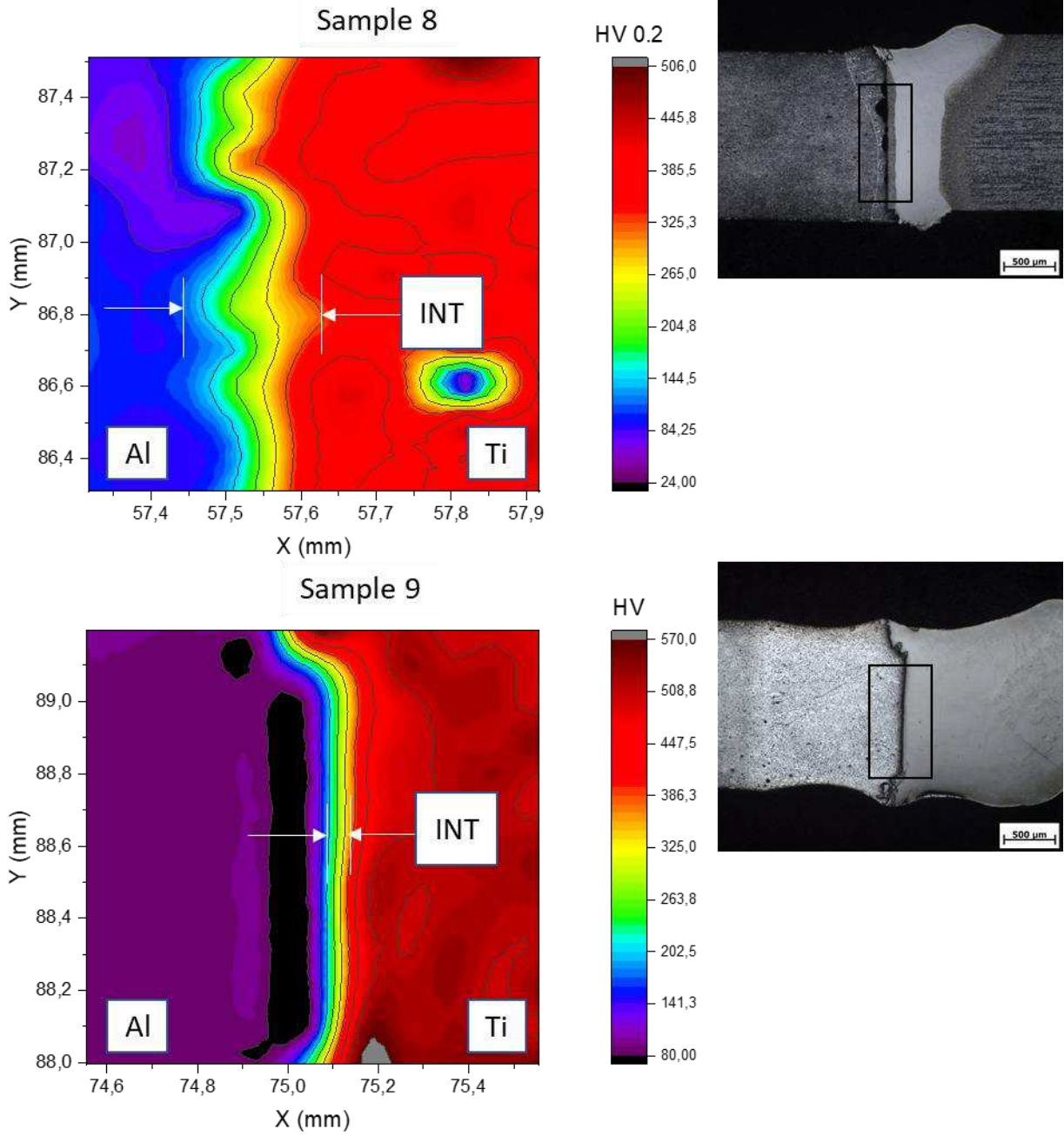


Figure 20 – Hardness values identified the analyzed regions and the interface of the test (INT) for the sample 8 and sample 9.

#### 4. Conclusions

The experiments carried out and the results obtained in this work aimed to investigate and optimize the weldability of the dissimilar joint AA6013 and Ti-6Al-4V obtained by the laser welding process. Therefore, based on the materials and methods used in this work, it can be concluded that:

1. Welding conditions: T1 (HI = 14.4 J/mm, Ws = 33.3 mm/s and offset = 0.5 mm), T6 (HI = 12.4 J/mm, Ws = 33.3 mm / if offset = 0.5 mm), T7 (HI = 9.6 J/mm, Ws = 50.0 mm / if offset = 0.3 mm) and T9 (HI = 24.0 J/mm, Ws = 16 , 6 mm/s and offset = 0.5 mm); did not show significant discontinuities in the weld bead, thus meeting the acceptance criteria of the AWS D17.1 standard.
2. The microstructure on the side of the aluminum alloy was characterized by the presence of  $\alpha$ -Al grains and dispersed precipitates inside the grains. Between the coarse-grained region of the heat-affected zone (HAZ) and the melted zone, dendritic cellular grains were formed. In the HAZ, next to the region that was partially fused, elongated grains with epitaxial growth were formed, as well as equiaxial grains. Columnar grains grew epitaxially from the melting line, while equiaxial grains were formed in the liquid phase in the solidification direction. In addition, the average grain size for T1 condition was 83% larger than the average grain size in T2. Likewise, the welding energy values associated with the offset also interfered with the dissolution and volumetric fraction of the precipitates. The molten zone region for the titanium alloy exhibited the  $\alpha'$  martensite phase, in addition to the secondary acicular phase. In the HAZ, a smaller volumetric fraction of  $\alpha'$  was formed as it moved away from the molten zone. In the region close to the Al/Ti interface, the phases  $\alpha$ ,  $\beta$  and a small amount of  $\alpha'$  were also identified. The volumetric fractions of  $\alpha$  were: 13, 18, 32 and 18% for samples T5, T6, T7 and T8 respectively. The volumetric fraction of  $\beta$  in this region increased as it was subjected to higher values of heat input.
3. Conditions T6 and T9 showed the highest values of tensile strength compared to the other experiments, around 60 and 50% (respectively) of the resistance of the aluminum alloy. The presence of the reactive layer between the titanium alloy and

the aluminum alloy along the joint, the curvilinear shape on the face and root, as well as the layer thickness of intermetallic compounds acted as agents, promoting coalescence. The main intermetallic compounds identified in these cases were: TiAl, Ti<sub>3</sub>Al<sub>4</sub>, Ti<sub>2</sub>Al<sub>3</sub> and Ti<sub>5</sub>Al<sub>3</sub>.

4. The hardness values for the molten zone on the Al side were not strongly affected by changes in offset and welding energy. The titanium alloy side, on the other hand, showed more heterogeneous hardness values, in addition to forming sites with high hardness values close to the junction interface, caused by the presence of intermetallic compounds. In addition, the hardness at the joint interface has been significantly changed due to the offset and the welding energy. For the same offset value and higher welding energy value, there was an increase in the hardness of the interface. An example is sample 9, in comparison to sample 1, with almost twice the welding energy, got a hardness increase value of 100 HV0.2.
5. In conclusion, the extension of the HAZ, the volumetric fraction of the phases and intermetallic compounds are associated with the value of the offset and the welding energy used in each condition of the experiments. Likewise, the appearance of the weld bead is closely related to the action that the molten metal (in this case, aluminum) had on wetting the titanium alloy interface.

## **Declarations**

**Funding:** This research received no external funding.

**Conflicts of Interest:** The authors declare no conflict of interest.

**Availability of data and materials:** Not applicable.

**Code availability:** Not applicable

**Author contributions:** Anderson Ribeiro, Milton Fernandes and Jorge Abdalla conceived and designed the laser welding experiments. Anderson Ribeiro, Milton Fernandes e Rafael de Siqueira performed the experiments. Anderson Ribeiro and Jorge Abdalla analyzed the data. Anderson Ribeiro and Rafael Giorjão discussed the results. Anderson Ribeiro wrote the paper. Anderson Ribeiro and Rafael Giorjão revised the manuscript.

**Ethical Approval:** Not applicable.

**Consent to participate and to publish:** All the authors mentioned in the manuscript have agreed for authorship, read and approved the manuscript, and given consent for submission and subsequent publication of the manuscript.

## References

1. Chen S, Li L, Chen Y, Huang J (2011) Joining mechanism of Ti/Al dissimilar alloys during laser welding-brazing process. *J Alloys Compd* 509:891–898. <https://doi.org/10.1016/j.jallcom.2010.09.125>
2. Kreimeyer M, Wagner F, Vollertsen F (2005) Laser processing of aluminum-titanium-tailored blanks. *Opt Lasers Eng* 43:1021–1035. <https://doi.org/10.1016/j.optlaseng.2004.07.005>
3. Naeem M (2006) Micro joining of dissimilar metals with a pulsed Nd: YAG laser. *PICALO 2006 - 2nd Pacific Int Conf Appl Laser Opt - Conf Proc* 323:323–328. <https://doi.org/10.2351/1.5056951>
4. Woizeschke P, Vollertsen F (2016) A strength-model for laser joined hybrid aluminum–titanium transition structures. *CIRP Ann - Manuf Technol*. <https://doi.org/10.1016/j.cirp.2016.04.027>
5. Miyagi M, Wang H, Yoshida R, et al (2018) Effect of alloy element on weld pool dynamics in laser welding of aluminum alloys. *Sci Rep*. <https://doi.org/10.1038/s41598-018-31350-4>
6. Zhou X, Duan J, Zhang F, Zhong S (2019) The study on mechanical strength of titanium-aluminum dissimilar butt joints by laser welding-brazing process. *Materials (Basel)* 12:. <https://doi.org/10.3390/ma12050712>
7. Woizeschke, P.; Schumacher, J.; Specht, U.; Lang, A.; Vollertsen F (2014) Joining of Aluminum and Cfrp Parts Using Titanium Foils As Transition Elements. *Euro Hybrid Mater Struct* 2014 69–75
8. Gao M, Chen C, Gu Y, Zeng X (2014) Microstructure and tensile behavior of laser arc hybrid welded dissimilar Al and Ti alloys. *Materials (Basel)* 7:1590–1602. <https://doi.org/10.3390/ma7031590>
9. Rathod DB, Jain RA (2019) A Review on Dissimilar Friction Stir Welding of Aluminum Alloys to Titanium Alloys. In: *Innovations in Infrastructure: Proceedings of ICIF 2018*. Springer Singapore
10. Chen Y, Chen S, Li L (2010) Influence of interfacial reaction layer morphologies on crack initiation and propagation in Ti/Al joint by laser welding-brazing. *Mater Des* 31:227–233. <https://doi.org/10.1016/j.matdes.2009.06.029>
11. H. Li; J.J Dai (2016) Research on dissimilar metal fusion welding – brazing of titanium alloy and aluminum alloy. In: Ping Chen (Department of Electrical and Computer Engineering, Boise State University U (ed) *Material Science and Engineering: Proceedings of the 3rd Annual 2015 International Conference on Material Science and Engineering (ICMSE2015)*, Guangzhou, Guangdong, China, 15-17 May 2015, Material S. Taylo & Francis Group, London, UK, pp 53–56
12. Sahul M, Sahul M, Vyskoč M, et al (2017) Disk Laser Weld Brazing of AW5083 Aluminum Alloy with Titanium Grade 2. *J Mater Eng Perform* 26:1346–1357.

<https://doi.org/10.1007/s11665-017-2529-6>

13. Majumdar B, Galun R, Weisheit A, Mordike BL (1997) Formation of a crack-free joint between Ti alloy and Al alloy by using a high-power CO<sub>2</sub> laser. *J Mater Sci* 32:6191–6200. <https://doi.org/10.1023/A:1018620723793>
14. Ozaki H, Hayashi S, Kutsuna M (2009) Laser roll welding of dissimilar metal joint of titanium to aluminium alloy. *Weld Int* 23:501–509. <https://doi.org/10.1080/09507110802543005>
15. Jiangwei R, Yajiang L, Tao F (2002) Microstructure characteristics in the interface zone of Ti/Al diffusion bonding. *Mater Lett* 56:647–652. [https://doi.org/10.1016/S0167-577X\(02\)00570-0](https://doi.org/10.1016/S0167-577X(02)00570-0)
16. Havlík P, Kouřil J, Foret R, et al (2017) Evaluation of weldability of titanium alloy Ti-6Al-4V and aluminum alloy 6061 produced by electron beam welding. *Mater Sci Forum* 879:714–719. <https://doi.org/10.4028/www.scientific.net/MSF.879.714>
17. Choi JW, Liu H, Fujii H (2018) Dissimilar friction stir welding of pure Ti and pure Al. *Mater Sci Eng A* 730:168–176. <https://doi.org/10.1016/j.msea.2018.05.117>
18. Huang Y, Lv Z, Wan L, et al (2017) A new method of hybrid friction stir welding assisted by friction surfacing for joining dissimilar Ti/Al alloy. *Mater Lett* 207:172–175. <https://doi.org/10.1016/j.matlet.2017.07.081>
19. Li B, Zhang Z, Shen Y, et al (2014) Dissimilar friction stir welding of Ti-6Al-4V alloy and aluminum alloy employing a modified butt joint configuration: Influences of process variables on the weld interfaces and tensile properties. *Mater Des* 53:838–848. <https://doi.org/10.1016/j.matdes.2013.07.019>
20. Song Z, Nakata K, Wu A, et al (2014) Influence of probe offset distance on interfacial microstructure and mechanical properties of friction stir butt welded joint of Ti6Al4V and A6061 dissimilar alloys. *Mater Des* 57:269–278. <https://doi.org/10.1016/j.matdes.2013.12.040>
21. Plaine AH, Suhuddin UFH, Afonso CRM, et al (2016) Interface formation and properties of friction spot welded joints of AA5754 and Ti6Al4V alloys. *Mater Des* 93:224–231. <https://doi.org/10.1016/j.matdes.2015.12.170>
22. Zhang CQ, Robson JD, Prangnell PB (2016) Dissimilar ultrasonic spot welding of aerospace aluminum alloy AA2139 to titanium alloy TiAl6V4. *J Mater Process Technol* 231:382–388. <https://doi.org/10.1016/j.jmatprotec.2016.01.008>
23. Peyre P, Berthe L, Dal M, et al (2014) Generation and characterization of T40/A5754 interfaces with lasers. *J Mater Process Technol* 214:1946–1953. <https://doi.org/10.1016/j.jmatprotec.2014.04.019>
24. Chen Y, Chen S, Li L (2009) Effects of heat input on microstructure and mechanical property of Al/Ti joints by rectangular spot laser welding-brazing method. *Int J Adv Manuf Technol* 44:265–272. <https://doi.org/10.1007/s00170-008-1837-2>

25. Casalino G, Mortello M, Peyre P (2015) Yb-YAG laser offset welding of AA5754 and T40 butt joint. *J Mater Process Technol* 223:139–149. <https://doi.org/10.1016/j.jmatprotec.2015.04.003>
26. Tomashchuk I, Sallamand P, Cicala E, et al (2014) Direct keyhole laser welding of aluminum alloy AA5754 to titanium alloy Ti6Al4V To cite this version : *Science Arts & Métiers ( SAM )*
27. Song Z, Nakata K, Wu A, Liao J (2013) Interfacial microstructure and mechanical property of Ti6Al4V/A6061 dissimilar joint by direct laser brazing without filler metal and groove. *Mater Sci Eng A* 560:111–120. <https://doi.org/10.1016/j.msea.2012.09.044>
28. Vaidya W V., Horstmann M, Ventzke V, et al (2010) Improving interfacial properties of a laser beam welded Dissimilar joint of aluminium AA6056 and titanium Ti6Al4V for aeronautical applications. *J Mater Sci* 45:6242–6254. <https://doi.org/10.1007/s10853-010-4719-6>
29. The Aluminium Association (2015) International Alloy Designations and Chemical Composition Limits for Wrought Aluminum and Wrought Aluminum Alloys With Support for On-line Access From: Aluminum Extruders Council Use of the Information. Alum Assoc Arlington, Virginia 31
30. de Siqueira RHM, de Oliveira AC, Riva R, et al (2014) Mechanical and microstructural characterization of laser-welded joints of 6013-T4 aluminum alloy. *J Brazilian Soc Mech Sci Eng* 37:133–140. <https://doi.org/10.1007/s40430-014-0175-6>
31. ASTM B381 - 13 (2013) Standard Specification for Titanium and Titanium Alloy Forgings. Act Stand ASTM B381 02.04: <https://doi.org/10.1520/B0381>
32. D'Ostuni S, Leo P, Casalino G (2017) FEM simulation of dissimilar aluminum titanium fiber laser welding using 2D and 3D Gaussian heat sources. *Metals (Basel)* 7:.. <https://doi.org/10.3390/met7080307>
33. Elijah Kannatey-Asibu J (2009) *Principles of Laser Materials Processing*, 1st Ed. John Wiley & Sons, Inc, Hoboken, New Jersey
34. ASTM Standard E 8M-04 (2005) Standard test methods for tension testing of metallic material. West Conshohocken, PA
35. Hilton P, Blackburn J, Chong P (2007) Welding of Ti-6Al-4V with fibre delivered laser beams. 26th Int Congr Appl Lasers Electro-Optics, ICALEO 2007 - Congr Proc 1607:.. <https://doi.org/10.2351/1.5061019>
36. Matsunawa A, Kim J-D, Seto N, et al (1998) Dynamics of keyhole and molten pool in laser welding. *J Laser Appl* 10:247–254. <https://doi.org/10.2351/1.521858>
37. Pastor M, Zhao H, Martukanitz RP, Debroy T (1999) Porosity, underfill and magnesium loss during continuous wave Nd:YAG laser welding of thin plates of aluminum alloys 5182 and 5754. *Weld J (Miami, Fla)*

38. Tomashchuk I, Bendaoud I, Sallamand P, et al (2016) Multiphysical modelling of keyhole formation during dissimilar laser welding. Proc 2016 COMSOL Conf 1–7
39. Akbari M, Saedodin S, Toghraie D, et al (2014) Experimental and numerical investigation of temperature distribution and melt pool geometry during pulsed laser welding of Ti6Al4V alloy. Opt Laser Technol 59:52–59. <https://doi.org/10.1016/j.optlastec.2013.12.009>
40. Kurz W, Bezençon C, Gäumann M (2001) Columnar to equiaxed transition in solidification processing. Sci Technol Adv Mater 2:185–191. [https://doi.org/10.1016/S1468-6996\(01\)00047-X](https://doi.org/10.1016/S1468-6996(01)00047-X)
41. Zhao H, White DR, Debroy T (1999) Current issues and problems in laser welding of automotive aluminum alloys. Int Mater Rev 44:238–266. <https://doi.org/10.1179/095066099101528298>
42. Hakem M, Lebaili S, Mathieu S, et al (2019) Effect of microstructure and precipitation phenomena on the mechanical behavior of AA6061-T6 aluminum alloy weld. Int J Adv Manuf Technol 102:2907–2918. <https://doi.org/10.1007/s00170-019-03401-1>
43. Lin DC, Wang GX, Srivatsan TS (2003) A mechanism for the formation of equiaxed grains in welds of aluminum-lithium alloy 2090. Mater Sci Eng A 351:304–309. [https://doi.org/10.1016/S0921-5093\(02\)00858-4](https://doi.org/10.1016/S0921-5093(02)00858-4)
44. Christoph Leyens MP (2005) Titanium and Titanium Alloys Fundamentals and Applications. WILEY-VCH Verlag GmbH & Co. KGaA, Weinheim
45. Rafi HK, Karthik N V., Gong H, et al (2013) Microstructures and mechanical properties of Ti6Al4V parts fabricated by selective laser melting and electron beam melting. J Mater Eng Perform 22:3872–3883. <https://doi.org/10.1007/s11665-013-0658-0>
46. Elmer JW, Palmer TA, Babu SS, et al (2004) Phase transformation dynamics during welding of Ti-6Al-4V. J Appl Phys 95:8327–8339. <https://doi.org/10.1063/1.1737476>
47. Rai R, Elmer JW, Palmer TA, Debroy T (2007) Heat transfer and fluid flow during keyhole mode laser welding of tantalum, Ti-6Al-4V, 304L stainless steel and vanadium. J Phys D Appl Phys 40:5753–5766. <https://doi.org/10.1088/0022-3727/40/18/037>
48. Nikulina AA, Smirnov AI, Turichin GA, et al (2017) Special Features of the Structure of Laser-Welded Joints of Dissimilar Alloys Based on Titanium and Aluminum. Met Sci Heat Treat 59:534–539. <https://doi.org/10.1007/s11041-017-0185-y>
49. Blacha L, Mizera J, Folega P (2014) The effects of mass transfer in the liquid phase on the rate of aluminium evaporation from the Ti-6Al-7Nb alloy. Metalurgija 53:51–54
50. Casalino G, Mortello M (2016) Modeling and experimental analysis of fiber laser

offset welding of Al-Ti butt joints. *Int J Adv Manuf Technol* 83:89–98.  
<https://doi.org/10.1007/s00170-015-7562-8>

51. J. H. Westbrook (Brookline Technologies, Ballston Spa, New York, USA) and R. L. Fleischer (Union College, Schenactady, New York U (2000) *Crystal Structures of intermetallic compounds*. John Wiley & Sons, LTD, West Sussex, England
52. Gupta RK, Pant B (2018) Titanium aluminides. *Intermet Matrix Compos* 71–93.  
<https://doi.org/10.1016/b978-0-85709-346-2.00004-2>
53. Wang Q, Chen H, Zhu Z, et al (2016) A characterization of microstructure and mechanical properties of A6N01S-T5 aluminum alloy hybrid fiber laser-MIG welded joint. *Int J Adv Manuf Technol* 86:1375–1384.  
<https://doi.org/10.1007/s00170-015-8280-y>

# Figures

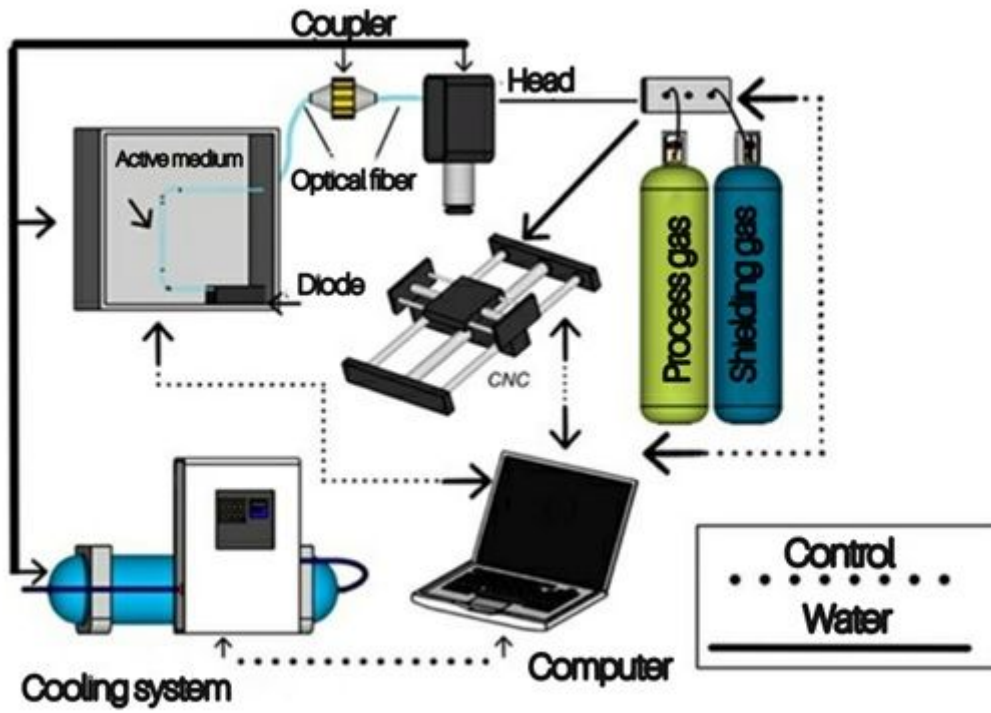
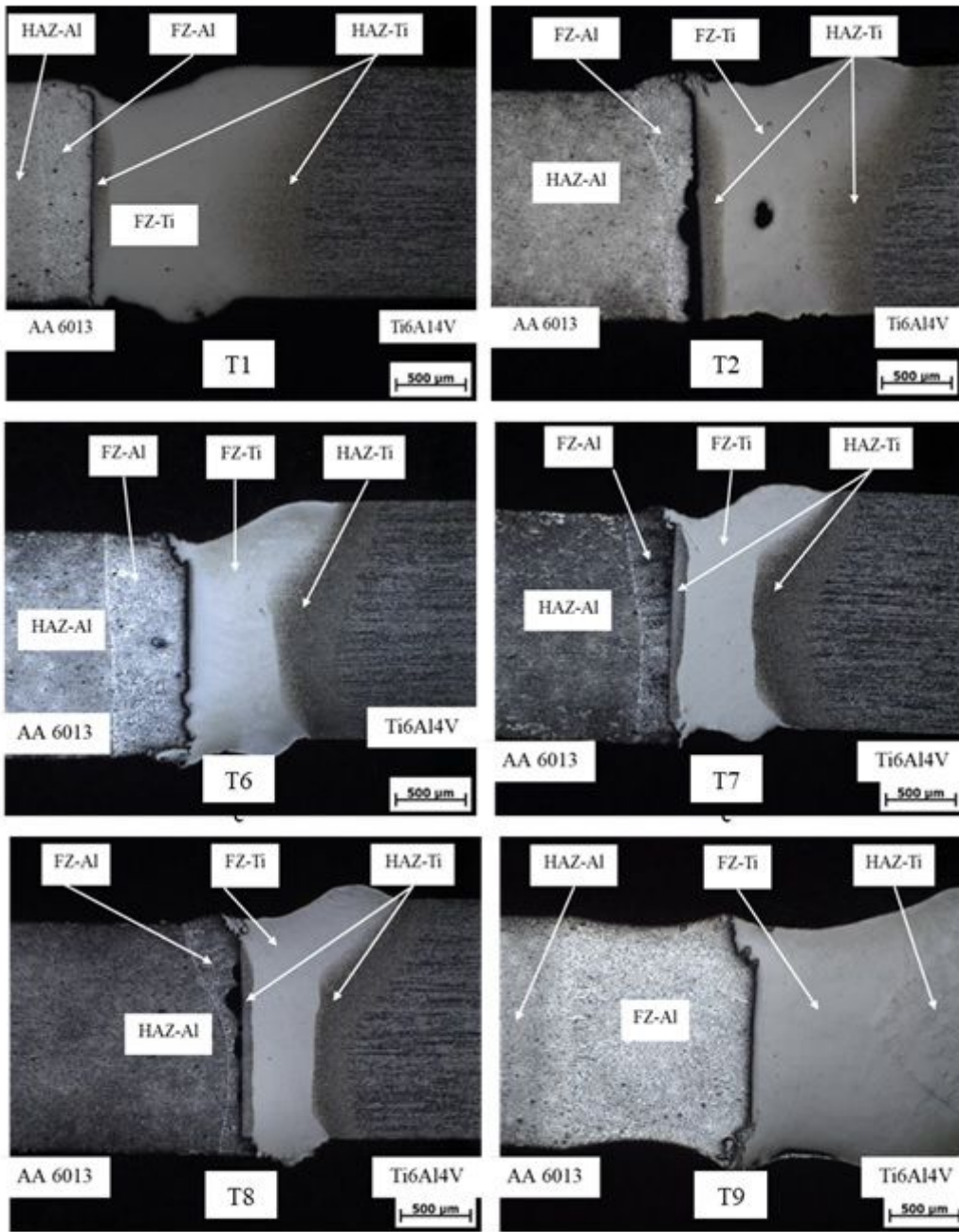


Figure 1

Schematic diagram of processing station with fiber laser



**Figure 2**

Details of the dissimilar joint of the samples: T1, T2, T6, T7, T8 and T9. Showing the region of the heat affected zone (HAZ) and fused zone (FZ). Original magnification 25x

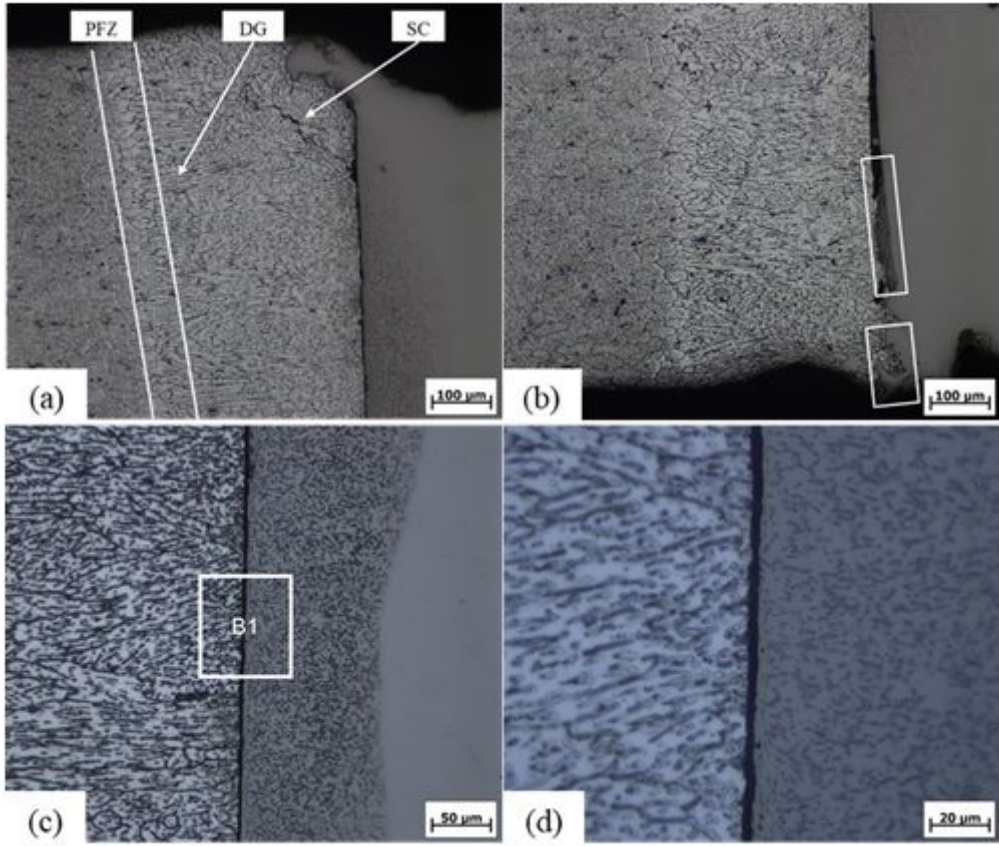


**Figure 3**

Microstructural characteristic at the welded joint for the T1 condition: a) partially fused zone (PFZ), dendritic grains (DG), cracking by solidification (SC); b) possible regions of intermetallic compound in the root; c) center of the cross section, d) region B1, original magnification 200x

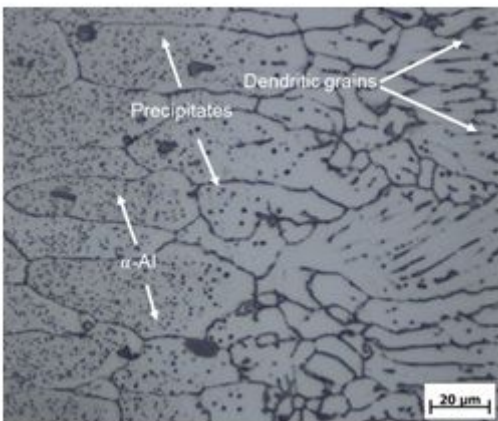


**Figure 4**

Sample T1, details at partially fused zone. Original magnification 500X

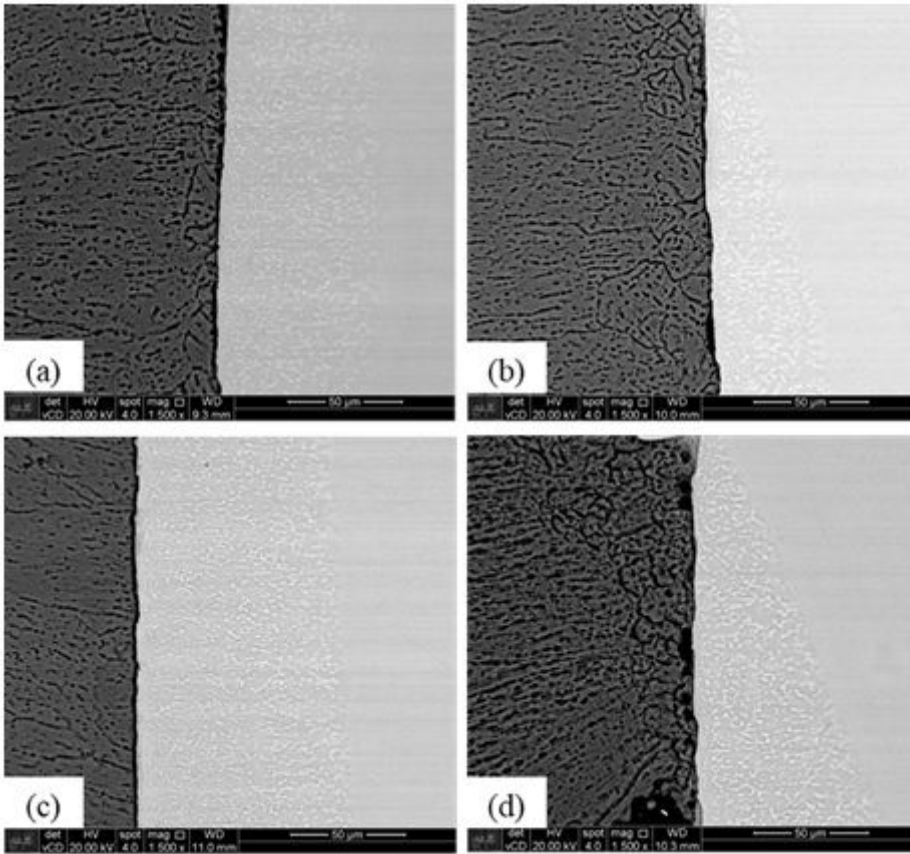


**Figure 5**

SEM image of the joint cross section center: a) condition T5, b) condition T6, c) condition T7 and d) condition T8

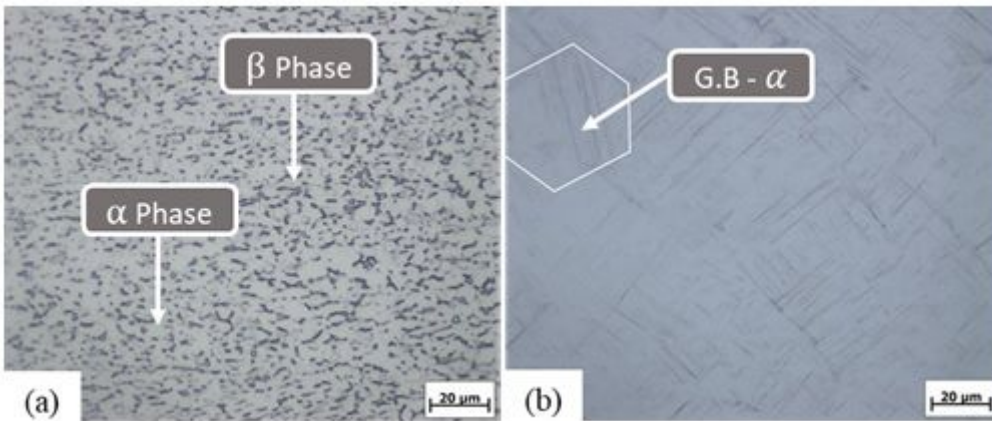


**Figure 6**

a) Microstructure of the base metal - titanium alloy (Ti-6Al-4V), original increase of 500x. b) Microstructure of the fused zone of the titanium alloy (Ti-6Al-4V), showing the  $\alpha'$  grain contour, original magnification 500x magnification

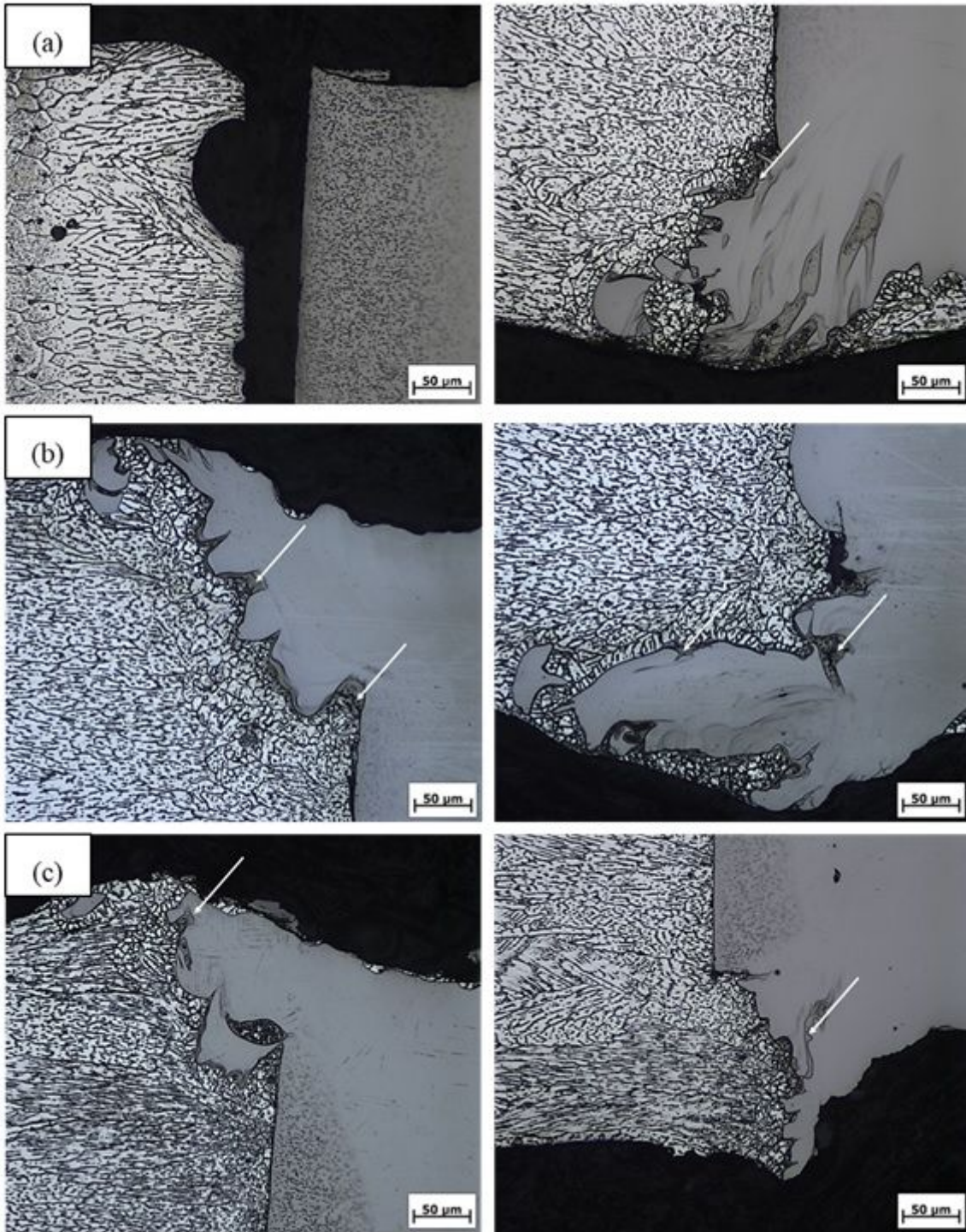


**Figure 7**

Regions with intermetallic compounds: Face (left) and root (right) of welded joints, (a) - Sample T2, (b) - Sample T6 and (c) - Sample T7.

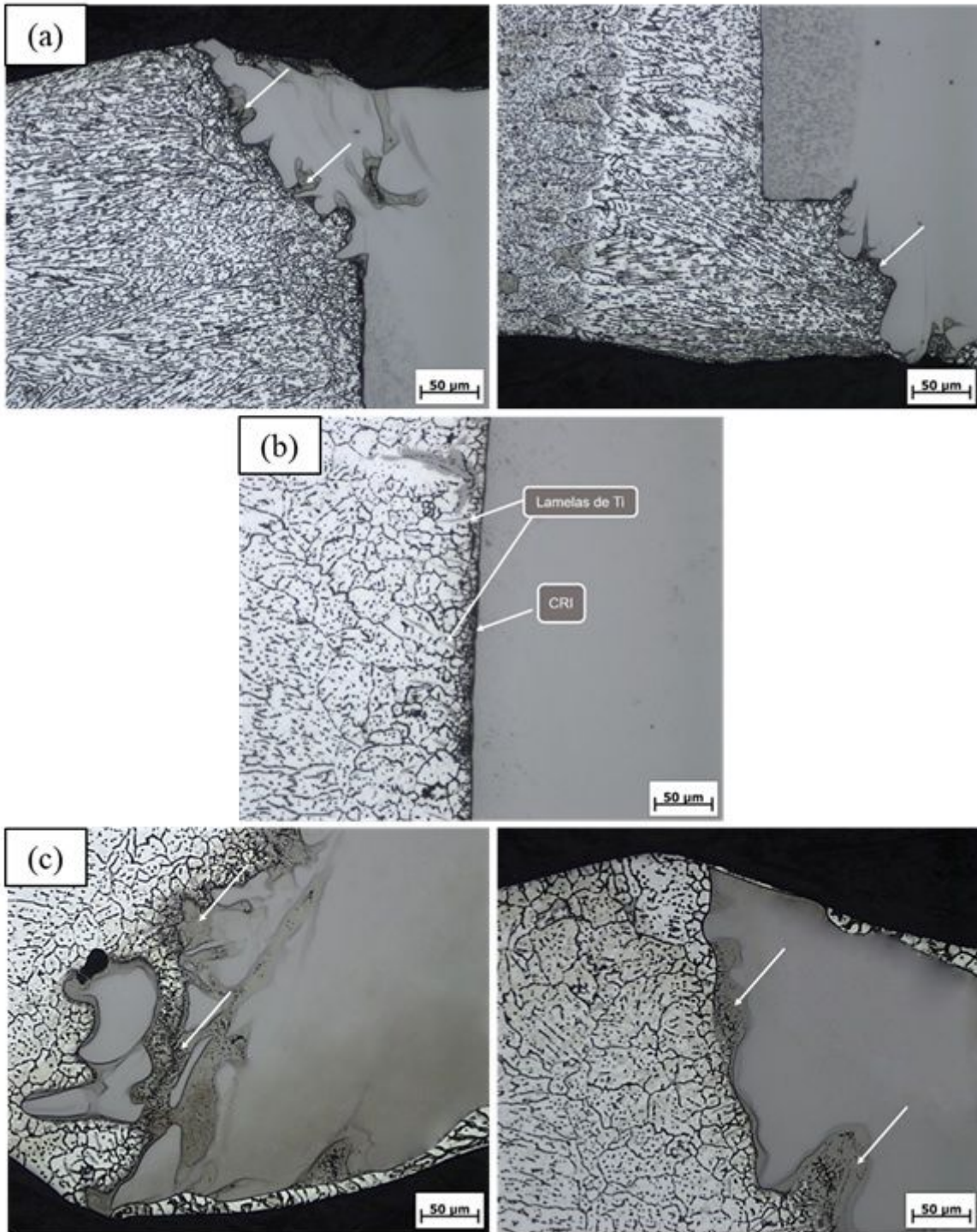


**Figure 8**

Regions with intermetallic compounds: (a) - Face (left) and root (right) of the welded joint, Sample T8. (b) - Center of the joint, Sample T9 and (c) - Face (left) and root (right) of the welded joint, Sample T9

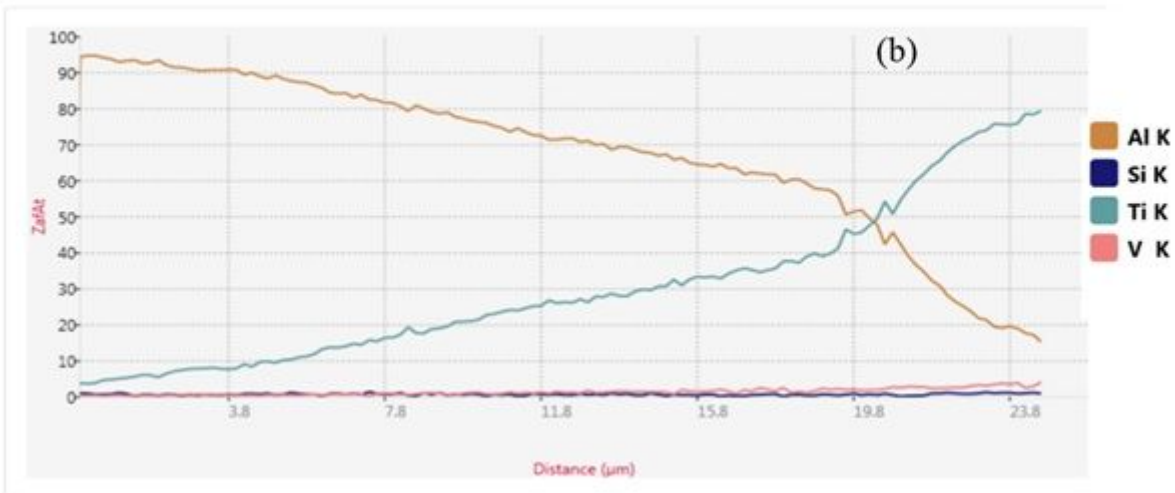
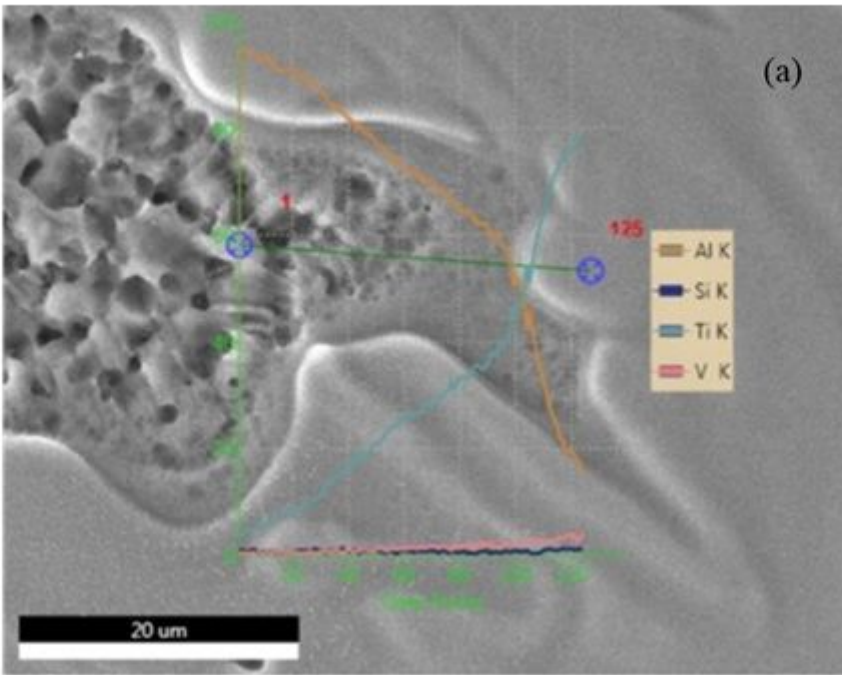


**Figure 9**

(a) Weld metal interface with path that EDS was carried out (b) Results of EDS analysis across Al/Ti welded interface

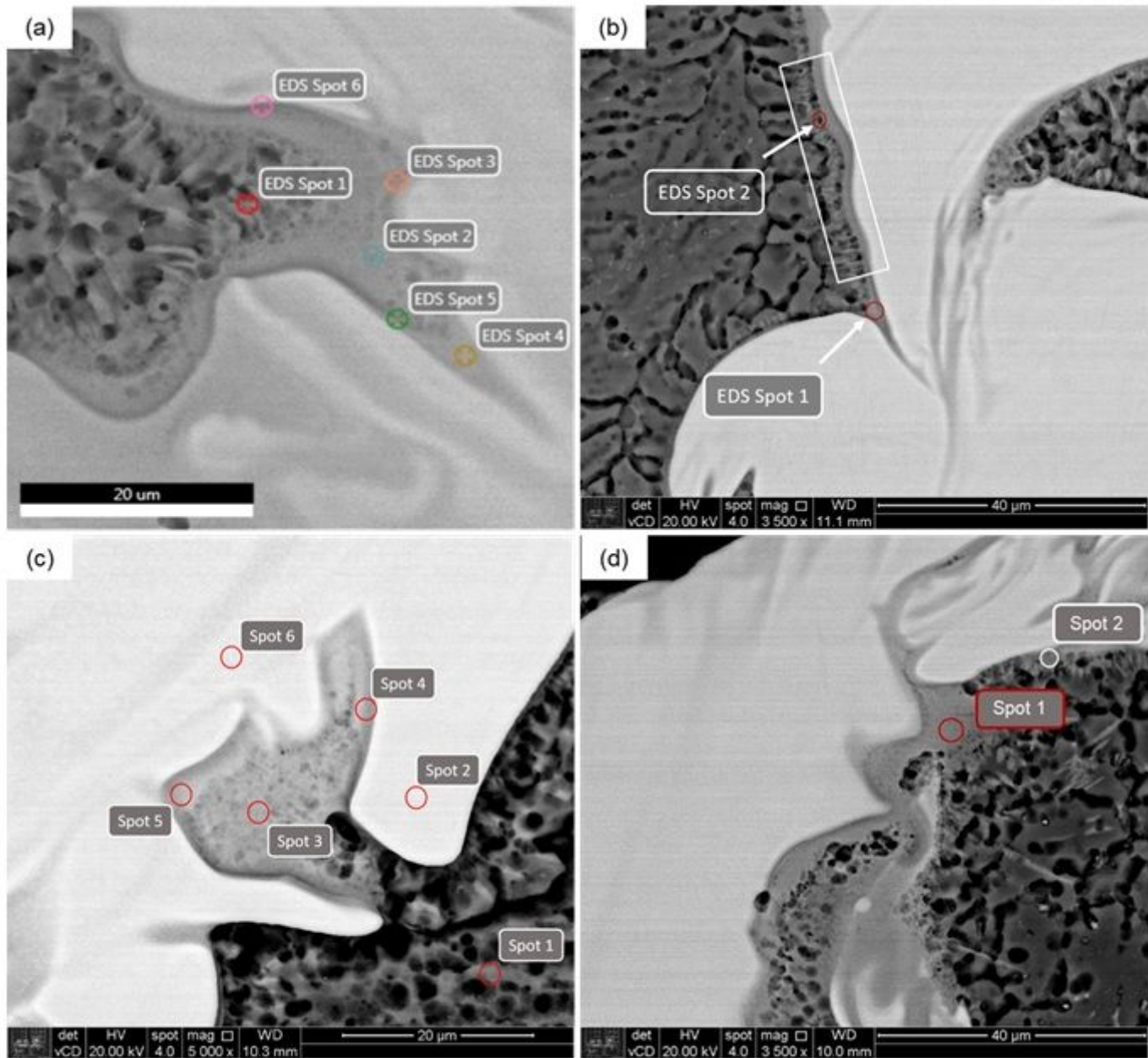


Figure 10

Points EDS analysis performed at (a) sample 6, (b) sample 7, (c) sample 8 and (d) sample 5

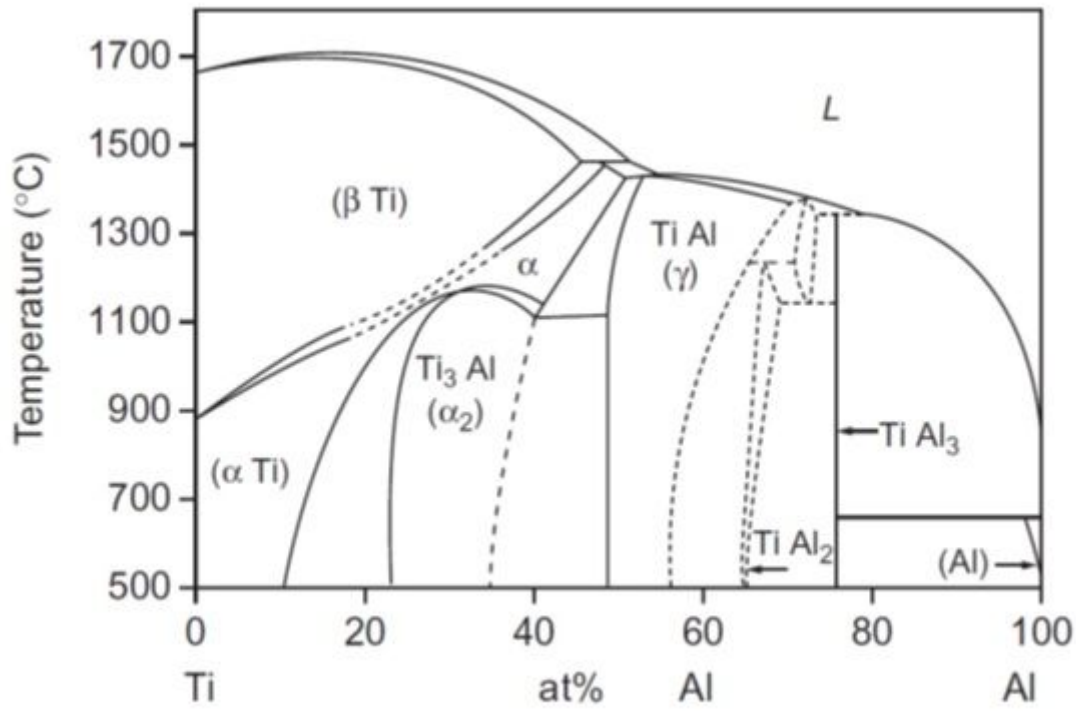


Figure 11

Phase diagram of the Ti-Al system[52]

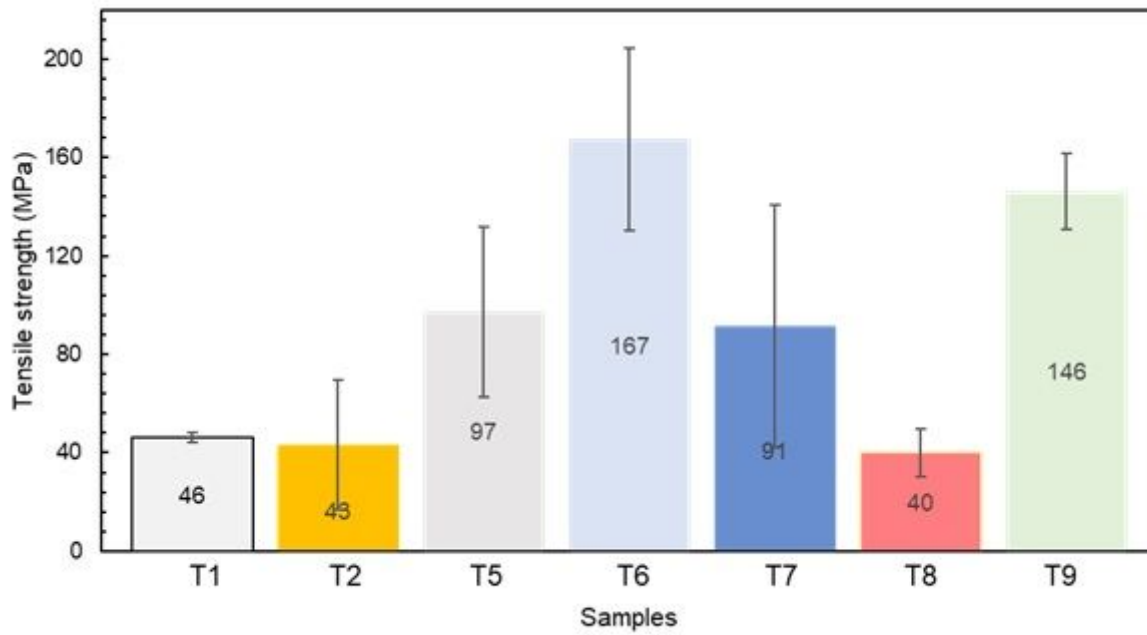
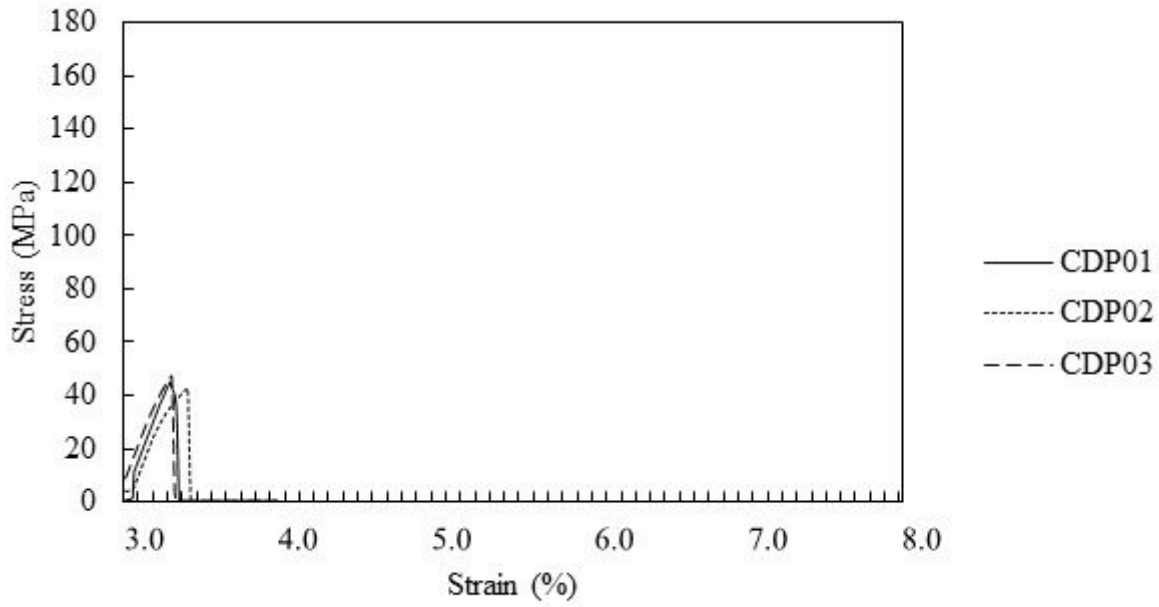


Figure 12

Average value of maximum tensile stress for each welded condition



**Figure 13**

Stress-strain curve - Sample T1

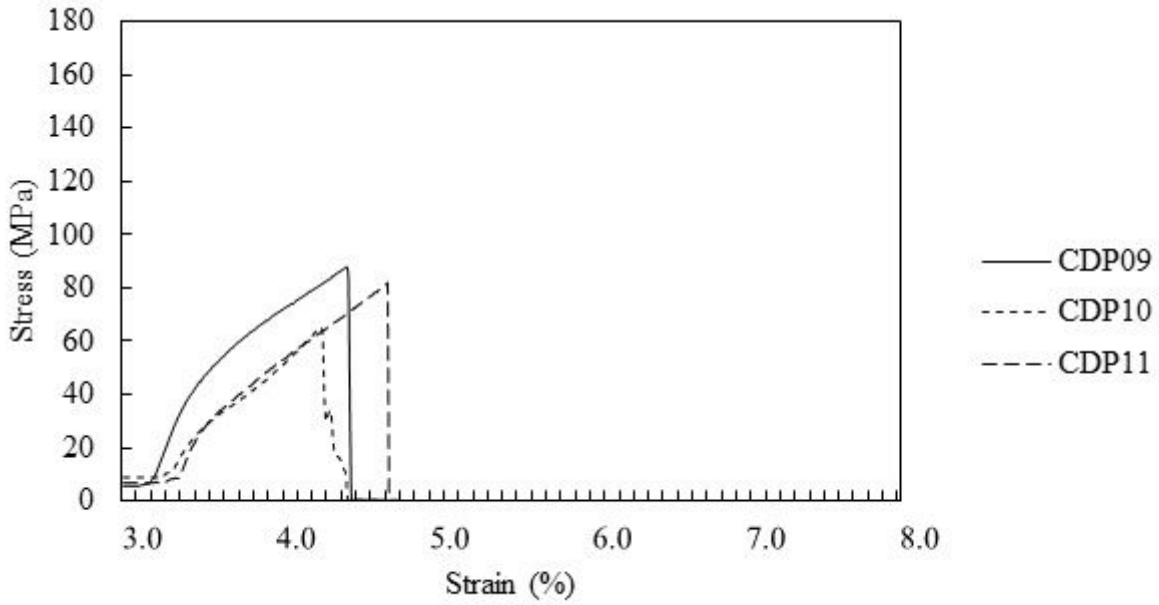


**Figure 14**

Stress-strain curve - Sample T5

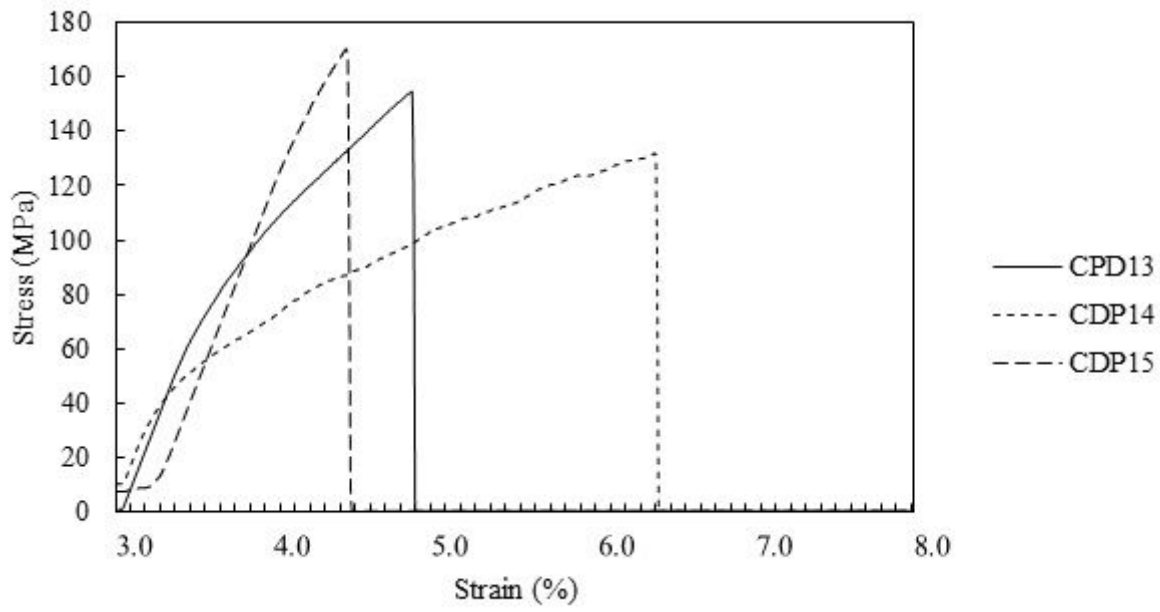


**Figure 15**

Stress-strain curve - Sample T6

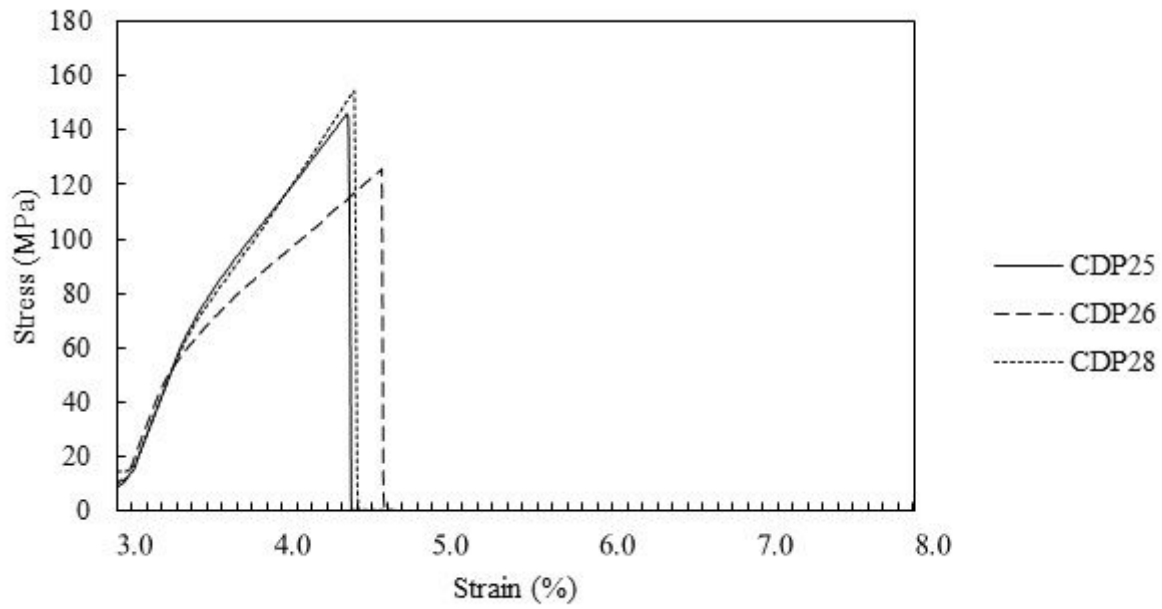


**Figure 16**

Stress-strain curve - Sample T9

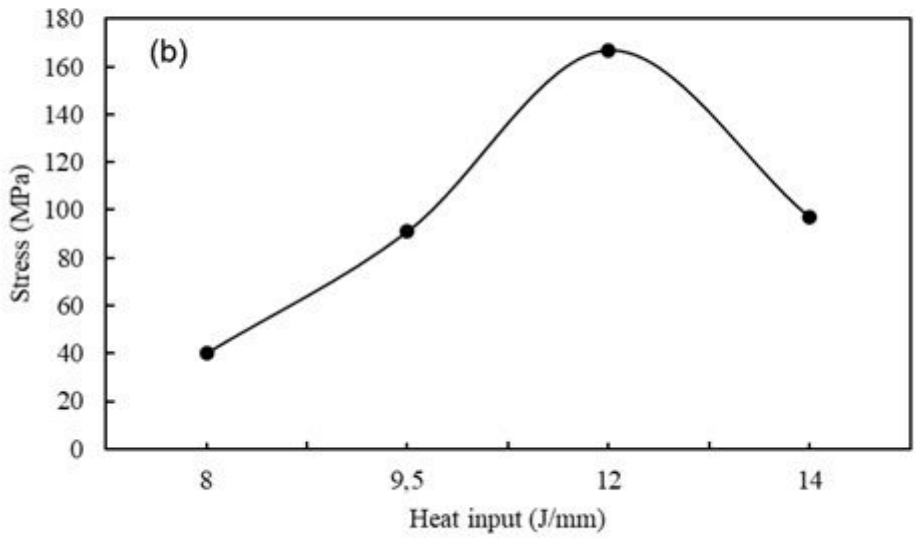
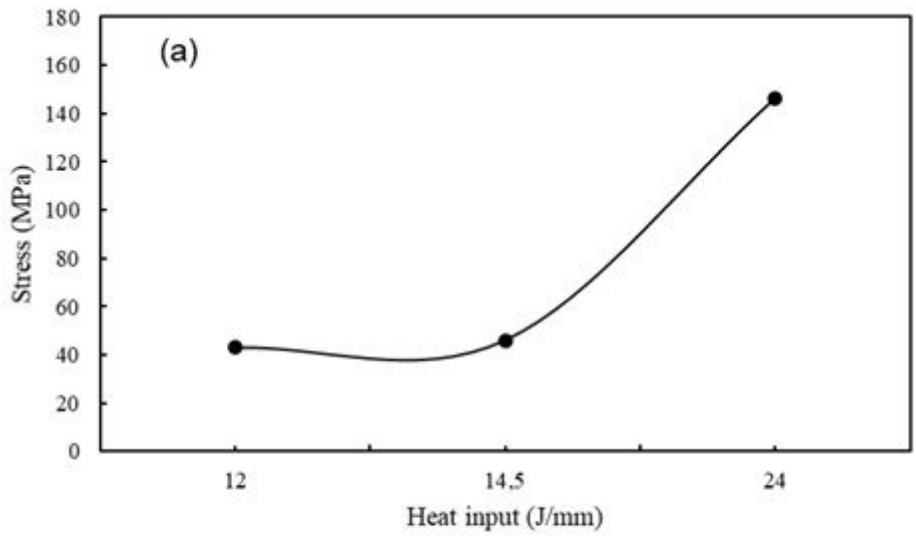


**Figure 17**

Tensile strength as a function of heat input: (a) Welding conditions for offset = 0.5 mm. (b) Welding conditions for offset = 0.3 mm.

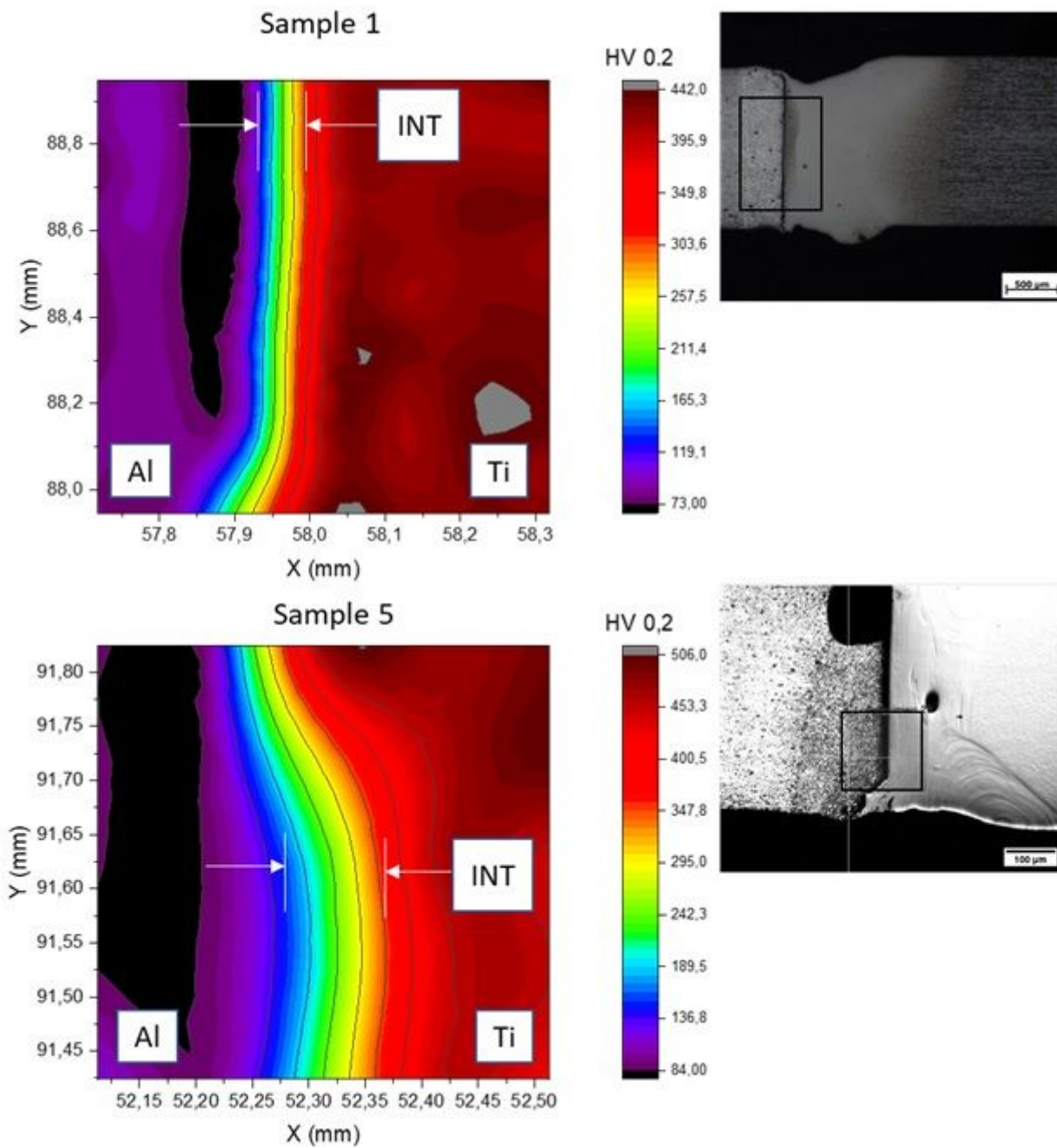


**Figure 18**

Hardness values identified the analyzed regions and the interface of the test (INT) for the sample 1 and sample 5.

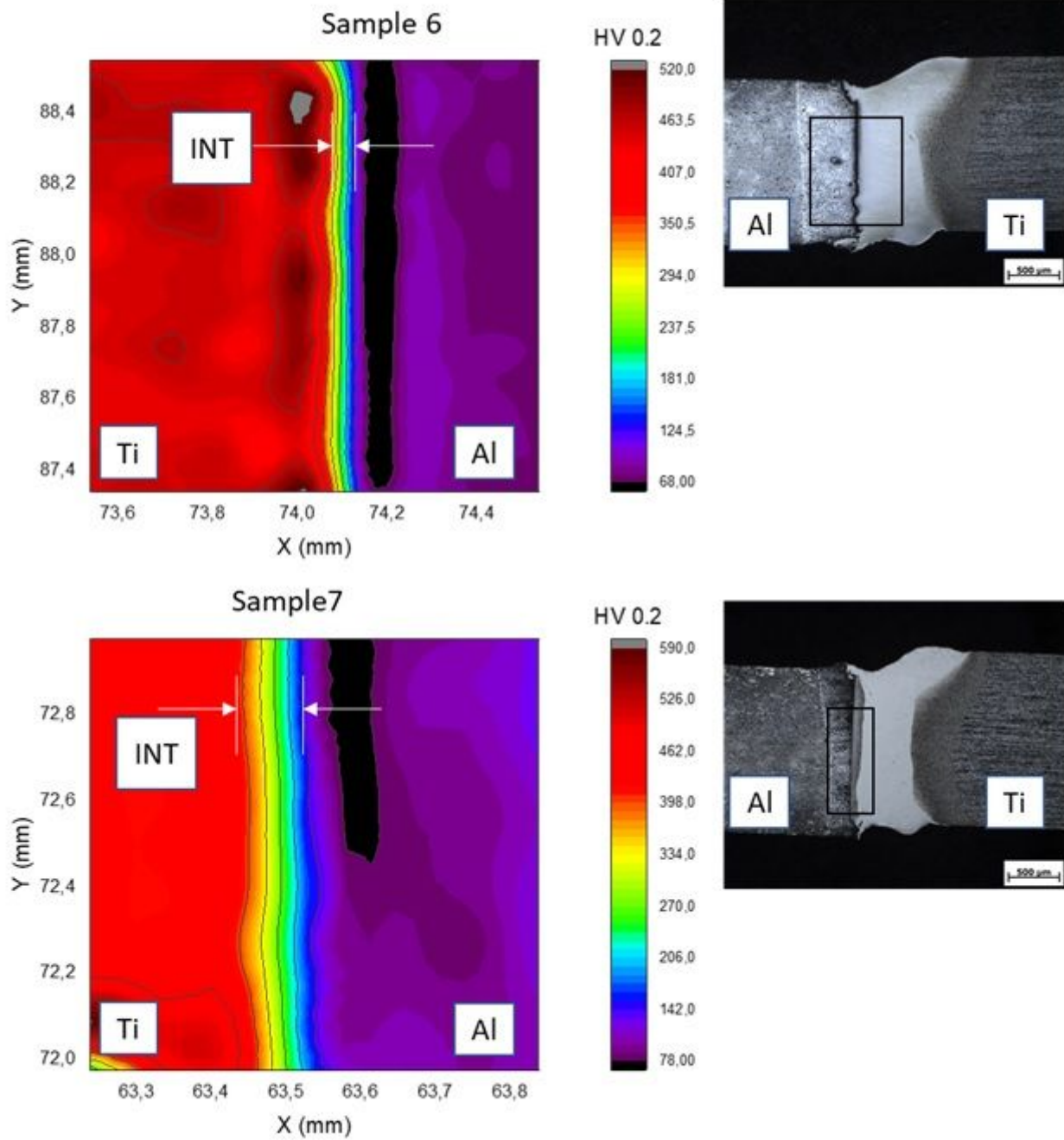


**Figure 19**

Hardness values identified the analyzed regions and the interface of the test (INT) for the sample 6 and sample 7.

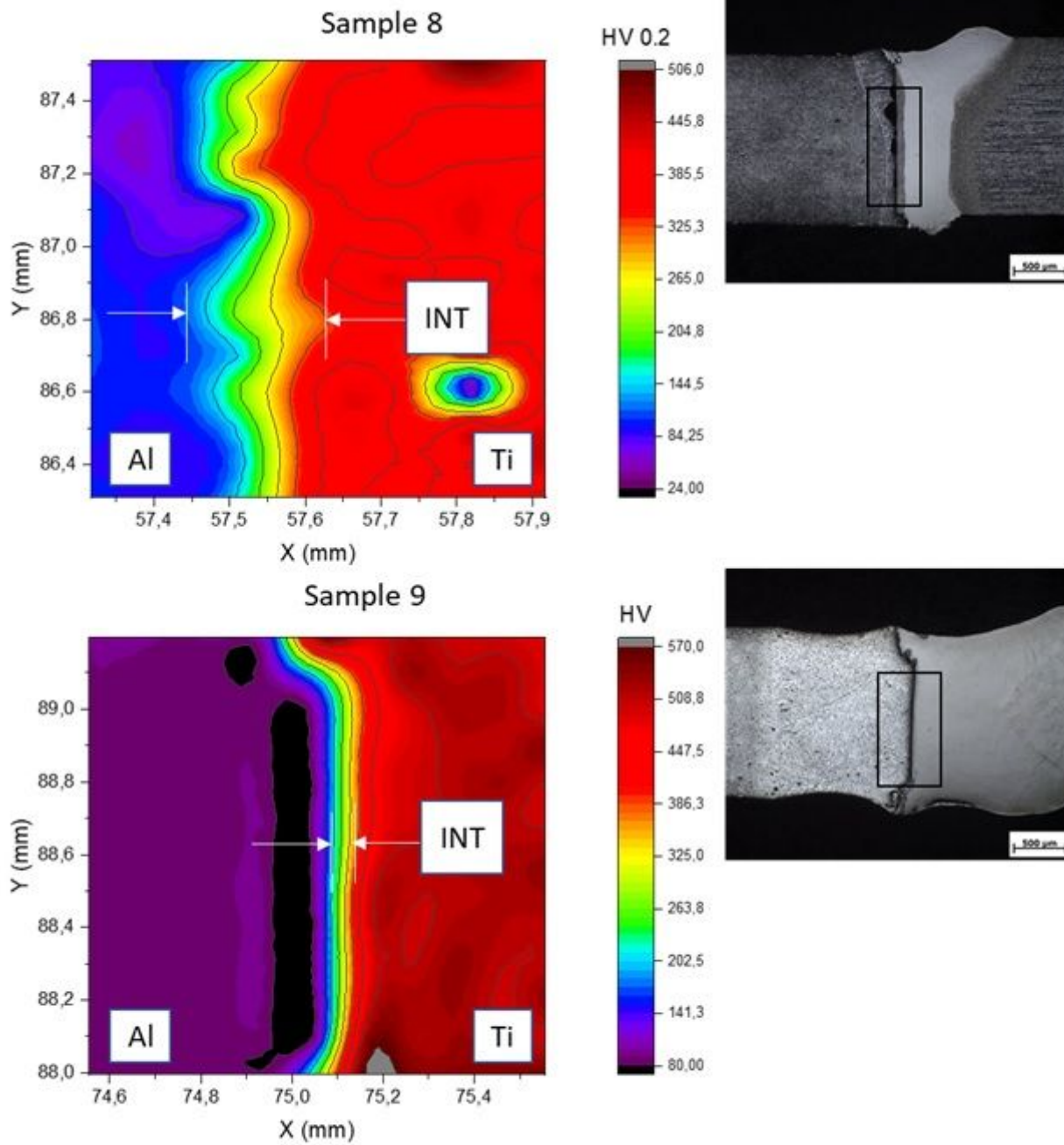


**Figure 20**

Hardness values identified the analyzed regions and the interface of the test (INT) for the sample 8 and sample 9.